

**PERLECAN KNOCKDOWN SIGNIFICANTLY ALTERS
EXTRACELLULAR MATRIX COMPOSITION AND ORGANIZATION
DURING CARTILAGE DEVELOPMENT**

by

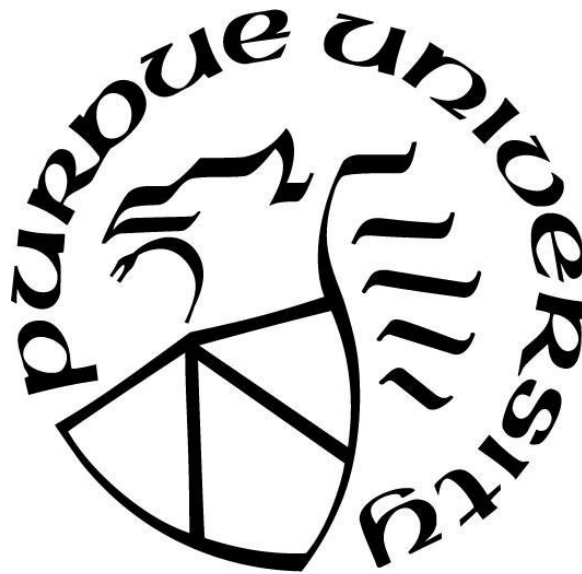
Alexander Robert Ocken

A Thesis

Submitted to the Faculty of Purdue University

In Partial Fulfillment of the Requirements for the degree of

Master of Science in Biomedical Engineering



Weldon School of Biomedical Engineering

West Lafayette, IN

May 2020

**THE PURDUE UNIVERSITY GRADUATE SCHOOL
STATEMENT OF COMMITTEE APPROVAL**

Dr. Sarah Calve, Chair

Weldon School of Biomedical Engineering, Purdue University
Department of Mechanical Engineering, University of Colorado Boulder

Dr. Tamara Kinzer-Ursem

Weldon School of Biomedical Engineering, Purdue University

Dr. Luis Solorio

Weldon School of Biomedical Engineering, Purdue University

Dr. Ashley W. Seifert

Department of Biology, University of Kentucky

Approved by:

Dr. George R. Wodicka

To my son,

May this work inspire him to fail gloriously, seek knowledge eagerly, and succeed humbly.

ACKNOWLEDGEMENTS

Without the guidance, knowledge, and love from the people mentioned below, this thesis would not exist. I would like to thank Dr. Kinzer Ursem and Dr. Luis Solorio, for their unrivaled mentorship; Dr. Sarah Calve, for instilling the attitude of a disciplined scientist; and Dr. Ashley W. Seifert, for inspiration to look for the weird and wonderful in this beautiful world. Also, my mentors, peers, and mentee: Nelda Vázquez and Tanaya Walimbe, Andrea Acuña and Kathryn Jacobson, and Madeline Ku. My family has endowed the traits I need to succeed. A competitive and inquisitive nature from my brother, sarcasm and the ability to view the world objectively from my sister, frugality and discipline from my father, and the intelligence and servant leadership from my mother. Lastly, Brittany's pure love, encouragement, and motivation made this journey possible.

TABLE OF CONTENTS

LIST OF FIGURES	7
ABSTRACT.....	8
ABBREVIATIONS	9
1. INTRODUCTION	10
1.1. Background	10
1.2. Significance.....	11
2. MATERIALS AND METHODS.....	13
2.1. Dissection of mouse distal humeral cartilage.....	13
2.2. Light microscopy methods.....	13
2.2.1. Immunofluorescent imaging	13
2.2.2. Safranin O staining	14
2.3. Biochemical assays	15
2.3.1. Dimethylmethylene blue (DMB) assay	15
2.3.2. Hydroxyproline (Hyp) assay.....	15
2.4. Proteomic methods.....	15
2.4.1. Protein and peptide sample preparation.....	15
2.4.2. Q-Exactive tandem mass spectrometry.....	16
2.4.3. Modification analyses	17
2.4.4. <i>Ex vivo</i> cartilage culture and secretome protein preparation	18
2.4.5. LC-MS/MS Statistical Analyses	18
2.5. TEM methods.....	19
2.5.1. Cartilage sample preparation and transmission electron microscopy.....	19
2.5.2. Fibril volume fraction and fibril diameter measurements.....	19
2.6. Modeling native cartilage.....	20
2.6.1. Cartilage tissue decellularization, imaging, and processing	20
2.6.2. Finite Element Analysis.....	21

3. RESULTS	22
3.1. The distribution of nidogen-2 and type X collagen were altered in a murine model of SJS.....	22
3.2. Perlecan knockdown affected GAG deposition at the articular surface of cartilage	23
3.3. Matrisome composition was disrupted in perlecan-deficient cartilage	24
3.4. Hydroxyproline and hydroxylysine modifications were not affected by perlecan knockdown.....	29
3.5. Perlecan knockdown did not affect collagen fibril diameter or volume fraction in developing cartilage	31
3.6. Perlecan knockdown led to increased protein secretion <i>ex vivo</i>	33
3.7. Chondrocyte volume increased in perlecan-deficient cartilage	34
4. DISCUSSION	37
4.1. Murine cartilage matrisome significantly changes during development	37
4.2. Perlecan knockdown decreases abundance of PCM proteins	38
4.3. Perlecan regulates endochondral ossification during cartilage development.....	38
4.4. Matrisome compensation in perlecan-deficient cartilage.....	39
4.5. Excess matrix is not incorporated into the ECM network of perlecan knockdown cartilage.....	40
4.6. Haploinsufficiency of perlecan alters developing cartilage matrisome	41
4.7. Perlecan supports articular cartilage mechanics by regulating GAG deposition	41
4.8. Perlecan knockdown affects chondrocyte geometry and mechanics	42
APPENDIX A. ADDITIONAL INFORMATION	44
APPENDIX B. SUPPLEMENTAL FIGURES	45
REFERENCES	51

LIST OF FIGURES

Fig. 3.1.	Nidogen-2 and type X collagen expression are altered in perlecan-deficient mice....	22
Fig. 3.2.	Perlecan knockdown affects glycosaminoglycan spatial distribution in P3 articular cartilage.....	24
Fig. 3.3.	Overview of the matrisome of developing murine cartilage.	27
Fig. 3.4.	Post-translational hydroxylation of collagens is not affected by perlecan knockdown.....	30
Fig. 3.5.	Perlecan knockdown does not substantially affect epiphyseal fiber architecture.	32
Fig. 3.6.	Perlecan knockdown affects cartilage secretome.	34
Fig. 3.7.	Individual chondrocyte volume significantly increased due to perlecan knockdown.	36
Fig. B.1.	Altered Nidogen-2 and type X collagen expression in perlecan-deficient mice.	45
Fig. B.2.	Workflow for proteomic analysis of developing murine cartilage.	47
Fig. B.3.	Cartilage composition significantly varies as a function of age and genotype.....	48
Fig. B.4.	Type I collagen expression in the developing epiphysis.	49
Fig. B.5.	Collagen banding patterns in developing cartilage.	49
Fig. B.6.	Cartilage secretome composition varies as a function of genotype.....	50

ABSTRACT

Functional repair of diseased or injured tissues remains a significant challenge for regenerative medicine. Extracellular matrix (ECM) composition during tissue assembly (*e.g.*, development) is dramatically different from that of the homeostatic adult and may aid the design of engineered therapeutics that will promote regrowth and functionality of damaged tissues. Implementing a top-down approach, we evaluated perlecan (HSPG2), a pericellular ECM protein critical for proper cartilage development. When HSPG2 is knocked down, the non-lethal phenotype mimics the musculoskeletal defects observed in human Schwartz-Jampel syndrome. We previously demonstrated that HSPG2 knockdown significantly decreased the stiffness of the interstitial matrix and chondrocytes in developing cartilage (Xu et al., 2016b). However, it is not clear what changes occur in ECM structure and organization to cause the observed decrease in stiffness when HSPG2 is knocked down. Therefore, we performed proteomic analysis using mass spectrometry to test the hypothesis that ECM components that contribute to the developing structural integrity of cartilage will be in lower abundance in *Hspg2*^{C1532Y-Neo} mutants (Neo/Neo) than in wildtype littermates (+/+). Relative increases in the abundance of ECM and associated proteins highlighted the expected developmental changes in ECM composition between embryonic day (E)16.5 and postnatal day (P)3 timepoints. The relative abundance of multiple proteins was significantly higher in Neo/Neo vs. +/+ P3 mice, contrasting our original hypothesis. Further investigation confirmed that the total collagen content increased with HSPG2 knockdown. However, similar collagen fibril diameter and ECM volume fractions between P3 Neo/Neo and +/+ littermates suggested HSPG2 knockdown did not affect matrix protein organization and assembly. Sulfated glycosaminoglycan (GAG) abundance showed no difference between groups, but safranin O staining indicated atypical GAG deposition. This, and increased hyaluronic acid binding protein expression, suggested increased hyaluronic acid deposition leads to decreased mechanical stiffness in Neo/Neo cartilage. Chondrocytes in perlecan-deficient cartilage may upregulate the synthesis of key ECM to compensate for decreased matrix stiffness; however, without HSPG2, GAGs accumulate and the matrix assembles into a structure with less mechanical integrity. Overall, the study of perlecan-deficient mice will provide insight into the influence of HSPG2 on chondrogenesis, matrix secretion, and functional cartilage assembly to enhance our design of engineering scaffolds that mimic cartilage to promote restoration of tissue function.

ABBREVIATIONS

Abbreviation	Terminology
A2MP	Alpha-2-macroglobulin-P
AFM	Atomic force microscopy
CHAD	Chondroadherin
COL1Ax	Type I collagen
COL2A1	Type II collagen
COL3A1	Type III collagen
COL5Ax	Type V collagen
COL9Ax	Type IX collagen (alpha x)
COL10A1	Type X collagen
COL11Ax	Type XI collagen (alpha x)
COL15A1	Type XV collagen
COMP	Cartilage oligomeric matrix protein
CTSB	Cathepsin B
CTSL	Cathepsin L1
DAPI	4',6-diamidino-2-phenylindole
DMB	Dimethylmethylene blue
E16.5	Embryonic day 16.5
P3	Postnatal day 3
ECM	Extracellular matrix
PCM	Pericellular matrix
ERK	Extracellular signal-regulated kinase
FDR	False discovery rate
FN1	Fibronectin
GAG	Glycosaminoglycan
sGAG	Sulfated GAG
HA	Hyaluronic acid
HABP	Hyaluronic acid binding protein
<i>Hspg2</i>	Perlecan encoding gene
HSPG2	Perlecan protein
Hyl	Hydroxylysine
Hyp	Hydroxyproline
LC-MS/MS	Liquid chromatography-tandem mass spectrometry
LEPREL1	Prolyl 3-hydroxylase 2
LEPREL2	Prolyl 3-hydroxylase 3
LFQ	Label-free quantification
LGALS3	Galectin-3
LOXLx	Lysyl oxidase homolog x
MATNx	Matrilin-x
MMP3	Matrix metalloproteinase-3
MOM	Mouse on mouse
+/+	Wildtype
Neo/+	Heterozygous <i>Hspg2</i> ^{C1532Y-Neo}
Neo/Neo	Homozygous <i>Hspg2</i> ^{C1532Y-Neo}
NID1	Nidogen-1
NID2	Nidogen-2
OCT	Optimal cutting temperature compound
OMD	Osteomodulin
PBS	Phosphate-buffered saline
PFA	Paraformaldehyde
PLODx	Lysyl hydroxylase x
POSTN	Periostin
ROI	Region of interest
RT	Room temperature
SDS	Sodium dodecyl sulfate
SERPINH1	Serpin H1
SJS	Schwartz-Jampel Syndrome
TEM	Transmission electron microscopy
TNC	Tenascin-C
WGA	Wheat germ agglutinin

1. INTRODUCTION

1.1. Background

The heparan sulfate proteoglycan perlecan is localized to the pericellular matrix (PCM) that surrounds chondrocytes in mature hyaline cartilage. Perlecan is a multifunctional and highly conserved protein known to affect the compressive modulus of the PCM (Guilak et al., 2006; Wilusz et al., 2012) and sequester growth factors (Farach-Carson et al., 2014; French et al., 1999; Vincent et al., 2007), indicating that it plays a role in both biomechanical and cell signaling. Mutations of the perlecan encoding gene, *Hspg2*, in humans result in defective endochondral ossification and skeletogenesis. Dissegmental dysplasia, Silverman-Handmaker type, is a lethal autosomal recessive disorder that presents with severe chondrodysplasia and dysmorphic facial features due to a null mutation in *Hspg2* (Arikawa-Hirasawa et al., 2001). Other mutations in *Hspg2* cause the non-lethal Schwartz-Jampel syndrome (SJS), which results in a decreased abundance of functional perlecan and leads to chondrodysplasia, myotonia, and early onset osteoarthritis (Nicole et al., 2000; Rodgers et al., 2007). While rare, these disorders are difficult to treat, and the current therapeutic focus is primarily symptom relief (Nessler et al., 2011).

Murine models generated to elucidate the function of perlecan during development have provided insight into disease progression and mechanisms underlying perlecan deficiency. Global knockout of *Hspg2* in mice is predominantly embryonic lethal, caused by myocardial basement membrane failure under mechanical stress (Costell et al., 1999). A model with the same point mutation as a form of SJS, *Hspg2*^{C1532Y-Neo}, produced mutant mice with similar phenotypes as found in humans, including growth plate defects and myotonia (Rodgers et al., 2007; Stum et al., 2008). A recent *in vitro* study, which used a fragment of perlecan with a common point mutation found in SJS, found that extracellular signal-regulated kinase (ERK) signaling was disrupted (Martinez et al., 2019). ERK is known to regulate the differentiation of cartilage to bone during development (Samsa et al., 2017), and the presence of intact perlecan may prevent endochondral ossification (Martinez et al., 2019). The absence of functional perlecan in SJS could lead to the activation of ERK signaling and explain why bone differentiation is accelerated. However, due to the multifaceted role of perlecan in regulating signaling within cells through both interactions with

the core protein and the sequestration of various growth factors (Gubbiotti et al., 2017; Vincent et al., 2007), there are likely many additional mechanisms that contribute to the SJS phenotype.

1.2. Significance

While studies often focus on the specific genetic mechanisms behind SJS, a comprehensive profiling of the developing extracellular matrix (ECM) may provide additional insight into how perlecan deficiency affects musculoskeletal functionality. When the initial skeletal template is specified in the embryo, perlecan and other ECM within the cartilage are less organized (Cescon et al., 2015; Xu et al., 2016b). As chondrogenesis progresses, perlecan and other PCM components (*e.g.*, type VI collagen, nidogens) become restricted to the periphery of the chondrocytes, taking on the organization characteristic of adult cartilage ECM. At the same time, chondrocytes increase synthesis of the bulk matrix, which is comprised of type II collagen fibers, glycosaminoglycans (GAGs), and proteoglycans, decreasing the overall volume fraction of cells (Han et al., 2011; Lycke et al., 2019). Chondrocytes either maintain the chondrogenic phenotype on the articulating surface to form mature hyaline cartilage or transition to bone within the rest of the skeletal template by first undergoing hypertrophy then endochondral ossification (Long and Linsenmayer, 1998). In perlecan-deficient mice, endochondral ossification and PCM formation are disrupted (Ishijima et al., 2012; Wilusz et al., 2012). Furthermore, we previously demonstrated that the compressive modulus of both cells and ECM is significantly decreased in the *Hspg2*^{C1532Y-Neo} mouse model (Xu et al., 2016b). Based on these observations, we hypothesized that perlecan knockdown would negatively affect the pericellular incorporation of perlecan binding partners, as well as dysregulate molecules that mediate proper ossification, leading to significant changes in ECM composition.

To test this hypothesis, we first visualized the distribution of key cartilaginous ECM proteins and GAGs in developing cartilage using immunohistochemistry, then assessed the proteome using liquid chromatography-tandem mass spectrometry (LC-MS/MS). We focused our analysis on the ECM proteins, termed the matrisome (Naba et al., 2012), to better elucidate and compare the composition of healthy and perlecan-deficient cartilage in embryonic and neonatal mice. We found that perlecan knockdown resulted in expected (*e.g.*, decrease in PCM components) and unexpected (*e.g.*, increase in bulk matrix) trends in ECM abundance. The ultrastructure of the ECM was not significantly different; however, more protein was secreted by *Hspg2*^{C1532Y-Neo} cartilage *in vitro*, suggesting that the ability of newly synthesized ECM to incorporate into the matrix was impaired.

Ultimately, perlecan knockdown prevents proper PCM formation and leads to ectopic ossification near the articulating surface (Arikawa-Hirasawa et al., 1999). These defects in ECM assembly due to perlecan deficiency result in the abnormal cartilage formation and osteoarthritis characteristic of SJS.

2. MATERIALS AND METHODS

All chemicals and reagents were acquired from Sigma-Aldrich (St. Louis, MO) unless otherwise specified.

2.1. Dissection of mouse distal humeral cartilage

Mice heterozygous for *Hspg2*^{C1532Y-Neo} (Neo/+) on a DBA background were provided by Dr. Sophie Nicole (Inserm, France) (Stum et al., 2008) and time mated to generate embryonic day (E)16.5 and postnatal day (P)3 mice. All murine experiments were approved by the Purdue Animal Care and Use Committee (PACUC; protocol 1310000973). Cartilage was dissected from the distal humerus of homozygous (Neo/Neo) and Neo/+ knockdown mice and wildtype (+/+) littermates (Fig. 3.1A). Care was taken to remove ligaments, bone, and ossified cartilage in the epiphyseal plate. Dissected cartilage was rinsed in phosphate-buffered saline (PBS), then immediately processed. Samples were either snap-frozen for proteomic and biochemical assays and stored at -80°C until used or fixed for transmission electron microscopy (TEM). Tail snips were used to confirm genotypes as previously described (Xu et al., 2016b).

2.2. Light microscopy methods

2.2.1. Immunofluorescent imaging

Forelimbs were embedded in Optimal Cutting Temperature compound (OCT, Sakura Finetek, St. Torrance, CA), frozen in dry ice-cooled isopentane, and stored at -80°C until sectioned. OCT embedded tissues were sectioned at 17µm and stored at -20°C. Before staining, sections were equilibrated to room temperature (RT), rehydrated with 1× PBS for 10 min, fixed with 4% paraformaldehyde (PFA) for 5 min, and rinsed with PBS. Then, sections were permeabilized with 0.1% Triton-X100 (Amresco, Cleveland, OH) in PBS and rinsed with 1× PBS. Background staining was reduced by using the Mouse on Mouse (MOM) staining kit (BMK-2022, Vector Labs, Burlingame, CA). Sections were incubated with MOM IG blocking buffer for 1 h and washed 3×2 min with PBS. Sections were primed with MOM protein diluent for 5 min before incubating with primary antibodies overnight and washed 3×2 min with PBS. Primary antibodies

against type X collagen (COL10A1, 1:50, X53 14-9771-80, Invitrogen, Carlsbad, CA), nidogen-2 (NID2, 1:50, sc-377424, Santa Cruz Biotechnology, Santa Cruz, CA), perlecan (HSPG2, 1:50, A7L6 sc-33707, Santa Cruz Biotechnology), type I collagen (1:100, AB765P, Millipore, Burlington, MA) and type II collagen (COL2A1, 1:100, MAB8887, Millipore) were diluted in MOM protein diluent. Biotinylated hyaluronic acid binding protein (HABP, 385911, Millipore) was diluted 1:150 in MOM protein diluent. Sections were primed again with MOM protein diluent for 5 min before staining with the appropriate secondary detection reagents [Goat anti-mouse IgG1 633 (1:500, Thermo Fisher Scientific, Rockford, IL), Goat anti-mouse IgG1 546 (1:500, Thermo Fisher Scientific), Donkey Anti-Rat IgG 488 (1:500, Thermo Fisher Scientific), Donkey Anti-Rabbit 647 (1:500, Thermo Fisher Scientific), Goat Anti-Mouse 546 (1:500, Thermo Fisher Scientific), phalloidin 555 (1:200, Thermo Fisher Scientific), Streptavidin 488 (1:500, Thermo Fisher Scientific), 4',6-diamidino-2-phenylindole (DAPI, 1:500, Roche, Fishers, IN)] in MOM protein diluent for 30 min in the dark. Incubations occurred at RT unless otherwise stated. Sections were mounted with Fluoromount-G (Electron Microscopy Sciences, Hatfield, PA) and imaged at 10× and 20× using a DMI6000 inverted microscope (Leica, Buffalo Grove, IL). The same acquisition parameters were used for all samples, and images were processed using FIJI (Rueden et al., 2017; Schindelin et al., 2012).

2.2.2. Safranin O staining

PFA fixed cryosections were stained with Harris' hematoxylin (Electron Microscopy Sciences) containing 4% glacial acetic acid (v/v) for 5 min, rinsed under tap water, and washed with PBS 2×10 min. Sections were stained with safranin O solution (0.1% safranin O w/v in H₂O, 0.22 μm pore vacuum filtered, Polysciences Inc., Warrington, PA) for 5 min, rinsed under tap water, and washed with PBS 3×10 min. Sections were mounted with Permount mounting medium (Electron Microscopy Sciences) and imaged at 10× and 20× using a DMI6000 inverted microscope.

2.3. Biochemical assays

2.3.1. Dimethylmethylene blue (DMB) assay

Glycosaminoglycans (GAGs) were extracted from distal humeral cartilage using a guanidine extraction buffer. Briefly, snap-frozen cartilage from right and left humeri was pooled (~1.5 and 2 mg wet-weight tissue from E16.5 and P3 cartilage, respectively) and pulverized using a tissue homogenizer (Ace Glass, 8325-08, Vineland, NJ) sitting in a liquid nitrogen bath. Pulverized samples were placed on ice for 15 min to allow the temperature to equilibrate. Samples were resuspended in 1 mL guanidine extraction buffer (4 M guanidine HCl, 50 mM sodium acetate, 100 mM N-ethylmaleimide, pH 5.8) by douncing twenty times with the homogenizer, transferred into 1.7 mL MaxyClear microtubes (Axygen, Union City, CA). Sulfated GAGs were assayed following (Hoemann, 2004). Briefly, 250 μ L of DMB solution (40 mM DMB, 40 mM NaCl, 40 mM Glycine, pH 3.00, 20 μ m filtered) was added to 10 μ L samples and 10 μ L 1 \times PBS with 1 mM ethylenediaminetetraacetic acid (PBE). Chondroitin 6-sulfate (shark cartilage, C4384) in PBE was used as a standard, adding 250 μ L of DMB solution to 10 μ L standards and 10 μ L guanidine extraction buffer. Optical density was measured at 530 and 590 nm, where the 590-baseline peak was subtracted from the 530 nm signal to increase assay sensitivity.

2.3.2. Hydroxyproline (Hyp) assay

Hyp was assayed from snap-frozen cartilage. Both humeri were pooled, dried at 110°C for 48 h, and weighed on a microbalance (~80 and 110 μ g dry-weight tissue from E16.5 and P3 cartilage, respectively). Hyp content was assessed using a Hyp assay kit (MAK008) according to the manufacturer's instructions. Water and HCl were added to maintain dry-weight tissue concentration at 4 μ g/ μ L (water or HCl).

2.4. Proteomic methods

2.4.1. Protein and peptide sample preparation

Protein was extracted from snap-frozen cartilage following Hsueh et al., 2016. Samples resuspended in guanidine extraction buffer were incubated 24 h on a rocking platform at 4°C and then reduced with 4 mM dithiothreitol for 30 min on an orbital shaker at 56°C and alkylated with 16 mM iodoacetamide for 1 h in the dark at RT. Extracts were ethanol precipitated (9:1 ethanol:

extract) overnight on a rocking platform at 4°C, followed by centrifugation at $13,750 \times g$ for 30 min at 4°C. Pellets were washed with cold ethanol for 4 h at -20°C and dried under vacuum. Extracts were resuspended in 500 μ L digestion buffer (100 mM Tris base, 2 mM calcium chloride, 10% acetonitrile v/v, pH 8.0), transferred to tissue homogenizers on ice, dounced twenty times, and returned to 1.7 mL microtubes.

Trypsin digestion was performed with 2.5 μ g MS grade trypsin (Thermo Fisher Scientific) per mg wet-weight tissue for 16 h on an orbital shaker at 37°C. Peptides were acidified with 1% trifluoroacetic acid (v/v) and ultra-filtrated using Ultra-micro C-18 SpinColumns (The Nest Group, Southboro, MA) according to the manufacturer's instructions. The eluent was dried using a CentriVap vacuum concentrator (Labconoco, Kansas City, MO) at 45°C and resuspended in 10 μ l running buffer (3% acetonitrile, 0.1% formic acid v/v). Peptide concentration was measured by 205 nm peptide absorbance using a NanoDrop 2000 spectrophotometer (Thermo Fisher Scientific) according to manufacturer's instructions and normalized to 0.2 mg/ml.

2.4.2. Q-Exactive tandem mass spectrometry

Trypsin-digested peptides equivalent to 1 μ g were analyzed with a Dionex UltiMate 3000 RSLC Nano System coupled to a Q Exactive™ HF Hybrid Quadrupole-Orbitrap Mass Spectrometer (Thermo Fisher Scientific). Primary spectra were collected from 400 to 1600 m/z at 120,000 resolution, a maximum injection time of 100 ms, and a dynamic exclusion of 15 s. The top 20 precursors were fragmented using higher-energy C-trap dissociation at a normalized collision energy of 27%. Tandem spectra were acquired in the Orbitrap at a resolution of 15,000 with a maximum injection time of 20 ms. Xcalibur RAW files were processed by MaxQuant (version 1.6.1.0) (Cox and Mann, 2008) to align primary spectra, identify proteins, and calculate relative protein abundance for LFQ. Tandem spectra were searched against the complete *Mus musculus* reference database (ID 000000589, downloaded from UniProt on 04/06/2018) comprising 53,127 proteins and a contaminants database. MaxQuant search parameters are tabulated in Supplemental Table 1. Variable modifications included oxidation of methionine, deamidation of asparagine, and hydroxylation of proline and lysine (Naba et al., 2017). Results were manually filtered, removing contaminants and proteins identified with only modified peptides or by reverse database matching, and requiring a minimum of two razor and unique

peptides across all sample replicates for identification and quantification. Raw data sets are available in the MassIVE repository (Ocken et al., 2019a).

2.4.3. Modification analyses

Hyp and hydroxylysine (Hyl) levels were analyzed by including them as variable modifications in MaxQuant. Analyses of hydroxylation were calculated from the MaxQuant evidence table outputs. Raw intensity (XIC) of each evidence (e) was multiplied by the number of modified residues ($m_{Mod,e}$) for a given modification, either Hyp or Hyl (Mod). These values were summed for each experiment (i). The summation was multiplied by the LFQ normalization coefficient (N_i) to give the normalized LFQ abundance of a modification for a given sample, $I_{Mod,LFQ,i}$ (Eq. 1).

$$I_{Mod,LFQ,i} = \sum_{e,i} (m_{Mod,e} * XIC_e) * N_i \quad (1)$$

Next, the number of prolines or lysines modified in each sample was calculated, using the ratio of modified to the total number of residues to calculate relative abundance. First, the number of modified residues ($m_{Mod,e}$) was divided by the total number of residues ($n_{Res,e}$) for a given modification, either Hyp and proline or Hyl and lysine (Res). This ratio was multiplied by the raw intensity of each evidence. These values were summed for each experiment to yield the relative intensity of modified to all residues, $I_{Mod,i}$ (Eq. 2).

$$I_{Mod,i} = \sum_{e,i} \left(\frac{m_{Mod,e}}{n_{Res,e}} * XIC_e \right) \quad (2)$$

Similarly, the relative intensity of unmodified to all residues was calculated, $I_{Unmod,i}$ (Eq. 3). In this case, one minus the ratio of modified to total residues was multiplied by each evidence raw intensity. This value was summed for each experiment.

$$I_{Unmod,i} = \sum_{e,i} \left(\left(1 - \frac{m_{Mod,e}}{n_{Res,e}} \right) * XIC_e \right) \quad (3)$$

Finally, the relative intensity of modified residues was divided by the total relative intensity of all residues and multiplied by the LFQ normalization coefficient (N_i) to give the LFQ normalized percent of modified residues for a given sample, $R_{Mod,LFQ,i}$ (Eq. 4).

$$R_{Mod,LFQ,i} = \frac{I_{Mod,i}}{I_{Mod,i} + I_{Unmod,i}} * N_i \quad (4)$$

2.4.4. *Ex vivo* cartilage culture and secretome protein preparation

Cartilage was cultured *ex vivo* following Wilson et al., 2016. Briefly, freshly dissected cartilage samples were washed in 70% ethanol and rinsed in PBS before being cultured in 0.5 mL serum-free, high glucose, HEPES-buffered Dulbecco's modified Eagle's medium with GlutaMAX (Gibco, Thermo Fisher Scientific), 50 mg/L 2-phospho-L-ascorbic trisodium salt, and 1% antibiotic/antimycotic. The supernatant for each culture was collected once after 48 h and again at the end of 96 h. At the end of the culture period, both the supernatant and cartilage samples were harvested separately and stored at -80°C until processed for LC-MS/MS.

The two aliquots of media were combined, precipitated with methanol-chloroform, and resuspended in 500 µL digestion buffer by douncing with a tissue homogenizer. Cartilage proteins were extracted as described above, whereas proteins in the supernatant were only reduced and alkylated. Then both sets of proteins were trypsin digested and analyzed by LC-MS/MS as described above. Peptide concentrations were assayed after resuspension in running buffer with a Pierce Quantitative Colorimetric Peptide assay (Thermo Fisher Scientific). Raw data sets are available in the MassIVE repository (Ocken et al., 2019b).

2.4.5. LC-MS/MS Statistical Analyses

Cartilage LC-MS/MS data were analyzed using SAS 9.4 (SAS Institute, Cary, NC) to evaluate the effect of development (one-way ANOVA) and perlecan knockdown (two-way ANOVA and post-hoc Tukey-adjusted simple effects multiple comparison test) using log₂-transformed LFQ intensities ($\alpha = 0.05$). One-way ANOVA was used when missing data prevented use of two-way ANOVA. Two-tailed Student's t-test was used when missing data prevented use of one-way ANOVA. This method was employed to incorporate degrees of freedom from all experimental groups when considering pairwise comparisons of interest (+/+; E16.5 vs. P3, E16.5: Neo/Neo vs. +/+, and P3: Neo/Neo vs. +/+). A false discovery rate (FDR) of 1% was applied to control false positives for multiple tests (Benjamini et al., 2006) using Prism 8.0.1 (GraphPad Software, La Jolla, CA).

Ex vivo explant LC-MS/MS data were analyzed in Prism to evaluate the effect of perlecan knockdown (2-tailed Student's t-test) using log₂-transformed values ($\alpha = 0.05$). Values were calculated by dividing the LFQ intensity by the summed total intensity for each sample. Results

were reported as an average of at least two biological replicates ($N = 3$). Similarly, Prism was used to apply 1% FDR.

2.5. TEM methods

2.5.1. Cartilage sample preparation and transmission electron microscopy

Freshly dissected cartilage samples were fixed in 2% PFA and 2% glutaraldehyde in 0.1 M cacodylate buffer overnight at 4°C. Fixed samples were rinsed with cacodylate buffer (3×5 min), impregnated with 1% osmium 0.8% ferricyanide for 1 h, rinsed in water (3×5 min), stained with 2% aqueous uranyl acetate for 30 min, and rinsed again with water (3×5 min). Samples were then ethanol dehydrated (50, 70, 95, 100% sequentially for 1×30, 1×30, 1×30, and 3×15 min, respectively) and transitioned to acetonitrile (2×15 min) before infiltration with Embed 812 (Electron Microscopy Sciences) and acetonitrile (2:1) for 2 h, (1:2) rotating overnight, and resin for 3 hours rotating. Samples were embedded in flat molds and cured overnight at 70°C in fresh resin. Ultrathin sections were cut at 85 nm with a 45-degree diamond knife (Diatome USA, Hatfield, PA) on a UC6 ultramicrotome (Leica), collected on 100 mesh formvar-coated copper grids, and post stained in 4% aqueous uranyl acetate and 2% aqueous lead citrate. Sections were imaged on an FEI T12 80kV TEM (FEI Company, Hillsboro, OR) in the Purdue Life Science Microscopy core facility.

2.5.2. Fibril volume fraction and fibril diameter measurements

Fibril volume fraction and diameter measurement protocols were adapted from Starborg et al., 2013. For fibril volume fraction measurements, uniform interstitial matrix regions between chondrocytes of the distal humeral cartilage were imaged at 30,000×. Three regions of interest (ROI) for both Neo/Neo and +/+ samples were segmented from each of $N = 4$ biological replicates using FIJI. The top layer of cells from the articular surface was excluded so that ROIs included only subsurface ultrastructure to avoid surface irregularities. The mean intensity of the ROI was divided by the maximum intensity range value (256) to calculate the fibril volume fraction percentage.

For fibril diameter measurements, uniform interstitial matrix regions were imaged at 120,000× magnification. ROIs were thresholded at the mean intensity. Individual fibrils, oriented

transversely, were manually fitted with the ellipse tool. The minor diameter was measured as the fibril diameter. Results for both fibril volume fractions and fibril diameters were averaged over the nine ROIs and reported as the average of the $N = 4$ biological replicates \pm standard deviation.

2.6. Modeling native cartilage

2.6.1. Cartilage tissue decellularization, imaging, and processing

Dissected humeri were decellularized in 0.05% sodium dodecyl sulfate (SDS) in PBS at RT with gentle rocking for 7 d (Lycke et al., 2019). The SDS solution was replaced every 24 h. Post-decellularization, samples were washed 3×30 min in PBS at RT and fixed in 4% PFA for 24 h at 4°C with gentle rocking. Samples were rinsed in PBS overnight at 4°C and transferred to fresh PBS for storage at 4°C until stained. Samples were incubated in blocking buffer [10% donkey serum (Lampire, Pipersville, PA) in PBS with 0.1% Triton X-100 (PBST)] for 24 h at 4°C with gentle rocking. Samples were stained with $20 \mu\text{g/mL}$ AlexaFluor488-tagged wheat germ agglutinin (WGA) (Thermo Fisher Scientific) diluted in blocking buffer for 48 h at 4°C with gentle rocking. Samples were washed 2×1 h with PBST at RT, then overnight at 4°C . Finally, samples were rinsed in PBS at 4°C for 1 h and transferred to fresh PBS for storage at 4°C until imaged.

Tissue samples were imaged using a $63\times$ oil-immersion plan-apochromat objective ($\text{NA} = 1.4$) on an LSM880 confocal microscope (Carl Zeiss, Oberkochen, Germany). Image stacks were acquired at 1024×1024 pixels, $2\times$ line averaged, with $0.22 \mu\text{m}/\text{pixel}$ xy -resolution and 0.75 or 0.39 μm z -axis intervals. The same image acquisition parameters were used for all samples. Three ROIs for both Neo/Neo and $+/+$ samples were segmented with the same dimensions ($28.55 \times 28.55 \times 28.50 \mu\text{m}$, $x \times y \times z$) from each of $N = 3$ biological replicates using FIJI. The top layer of cells from the articular surface was excluded so that ROIs included only subsurface cellular geometries to avoid surface irregularities and provide a consistent volume for comparison.

To calculate cartilage cell volumes and matrix volume fraction, a custom, automated ROI processing and segmentation algorithm developed in MATLAB to construct three-dimensional geometric models was used (Lycke et al., 2019). In brief, the algorithm-processed image stacks were enhanced using median filtering, histogram corrected to improve cell to ECM contrast, followed by adaptive thresholding (Otsu's method), morphological filtering, Chan-Vese active

contours, and watershed distance transform to segment cells from the rest of the volume. The resultant binary masks were used to calculate cell and matrix volume fractions.

2.6.2. Finite Element Analysis

To analyze the effect of developing cartilage mechanical properties and geometry, simulated compression was applied to three-dimensional ROIs using ANSYS version 19.0 (ANSYS, Inc., Canonsburg, PA) following (Lycke et al., 2019). Contact between cells and ECM geometries were bonded, and meshes for the finite element analysis had between 170,076 and 248,604 nodes and 99,688-146,073 elements with an average of 216,757 nodes and 127,610 elements per simulation. Cell and ECM compressive moduli were derived from atomic force microscopy (AFM) measurements of viable cartilage previously reported by Xu et al., 2016b. Poisson's ratios of 0.4 and 0.45 were applied to cells and ECM, respectively (Jin and Lewis, 2004; Trickey et al., 2006). Samples were compressed 5% tangential to the articulating surface towards the center of the cartilage. Equivalent von Mises stress and strain were measured for ECM and chondrocytes that were at least 1 μm from the ROI boundary.

3. RESULTS

3.1. The distribution of nidogen-2 and type X collagen were altered in a murine model of SJS

To determine how perlecan knockdown influences the ECM composition of cartilage, we analyzed the distal humerus of postnatal-day (P)3 mice, a period that captures the formation of distinct pericellular and bulk (or interstitial) matrices (Xu et al., 2016b). We used the *Hspg2*^{C1532Y-Neo} murine model in which perlecan secretion is reduced, leading to defects consistent with clinical manifestations of human SJS such as muscle stiffness and chondrodysplasia (Rodgers et al., 2007; Stum et al., 2008). First, to visualize how the organization of key ECM change, cryosections of P3 distal humeri were immunostained for nidogen-2 (NID2), a component of the PCM that binds with perlecan (Farach-Carson et al., 2014; Hopf et al., 1999), and type X collagen (COL10A1), a protein synthesized by hypertrophic chondrocytes (Gomes et al., 2002). The intensity of NID2 staining was lower in P3 homozygous (Neo/Neo) *Hspg2*^{C1532Y-Neo} mice compared to wildtype (+/+) mice in the epiphysis of the distal humerus (Figs. 3.1A, B; B.1). COL10A1 immunolocalization was increased in both the growth plate and epiphysis of Neo/Neo compared to +/+ littermates (Fig. 3.1C; B.1).

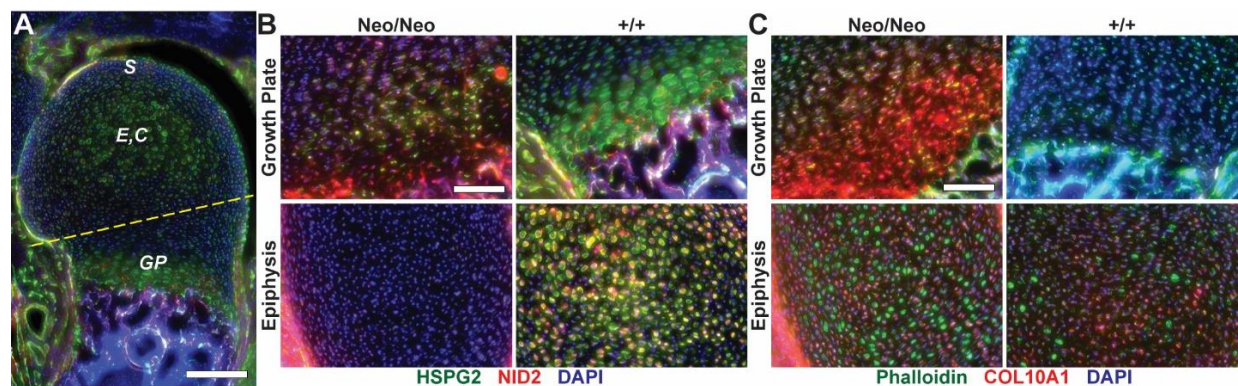


Fig. 3.1. Nidogen-2 and type X collagen expression are altered in perlecan-deficient mice. Immunofluorescent staining of P3 cartilage from the distal humerus. (A) Perlecan (green) staining in +/+ cartilage. The yellow dashed line indicates the dissection plane for biochemical and LC-MS/MS experiments. S: articular surface, E: epiphysis, C: center, GP: growth plate. (B) Perlecan (HSPG2; green) and nidogen-2 (NID2; red) staining was decreased in Neo/Neo growth plates and epiphyses. (C) There was an increase in type X collagen (COL10A1; red) in the growth plate and epiphysis of Neo/Neo mice compared to +/+ littermates, whereas there was no difference in actin organization as indicated by phalloidin staining (green). Nuclei were stained with (DAPI; blue). Scale bars: (A) 200 μm , (B, C) 100 μm . Images representative of N = 3 biological replicates.

3.2. Perlecan knockdown affected GAG deposition at the articular surface of cartilage

Combined with the observation that perlecan knockdown dysregulated ECM proteins crucial for proper cartilage development (Fig. 3.1) and previous reports that GAG deposition was increased in the intervertebral discs in *Hspg2* exon-3 null mice (Shu et al., 2019), we investigated whether the *Hspg2*^{C1532Y-Neo} mutation altered GAG abundance in hyaline cartilage. Cartilage was dissected from the distal humeri of P3 *+/+* and *Neo/Neo* mice, taking care to remove the growth plate (Fig. 3.1A). A dimethylmethylene blue (DMB) colorimetric assay, which quantifies sulfated GAG (sGAG) abundance, indicated no significant difference as a function of genotype (Fig. 3.2A). To confirm our biochemical results, we visualized the spatial distribution of GAGs with safranin O counterstained with hematoxylin. Surprisingly, the intensity of safranin O staining at the articulating surface of the cartilage varied between genotypes. For *Neo/Neo* mice, safranin O distribution was homogenous, decreasing only slightly near the articulating surface (Fig. 3.2B). In contrast, safranin O staining greatly diminished at the articulating surface of *+/+* cartilage, and the PCM surrounding individual chondrocytes was more pronounced compared to *Neo/Neo* mice (arrowheads, Fig. 3.2B). While the DMB assay specifically measures sGAG abundance, we hypothesized that the non-sulfated GAG hyaluronic acid (HA) was responsible for the profile revealed by safranin O, which stains all GAGs. Biotinylated-hyaluronic acid binding protein (HAPB) was used to visualize HA in the tissue and revealed a difference in the distribution between *Neo/Neo* and *+/+* samples. Specifically, HA was ubiquitously found in *Neo/Neo* cartilage, whereas it was decreased at the articulating surface in *+/+* animals (Fig. 3.2C). We also evaluated the expression of type II collagen (COL2A1), the major fibril forming collagen in cartilage, revealing elevated levels in perlecan-deficient mice (Fig. 3.2C). Overall, these histological data indicate that different components of both the PCM and bulk ECM were disrupted as a result of perlecan knockdown.

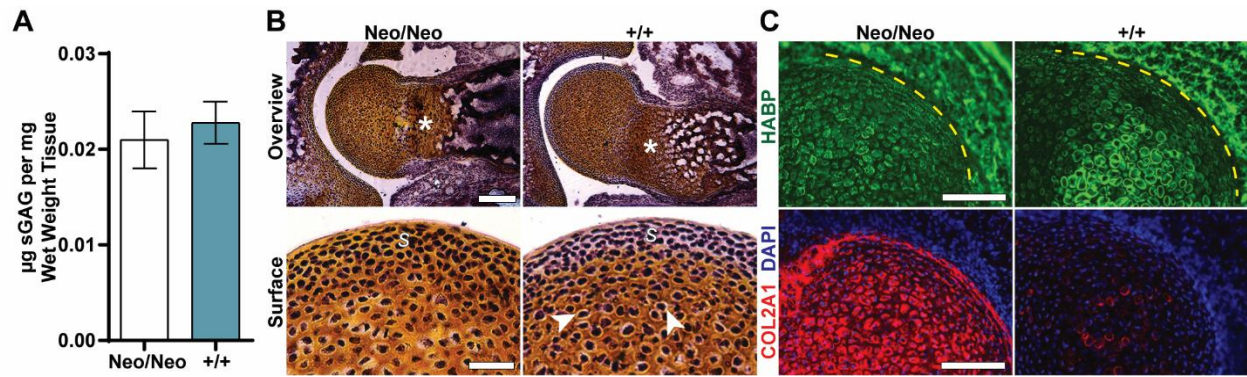


Fig. 3.2. Perlecan knockdown affects glycosaminoglycan spatial distribution in P3 articular cartilage. (A) A colorimetric assay for sulfated glycosaminoglycans (sGAG) indicated there was no significant difference in sGAG abundance between cartilage isolated from the humerus of Neo/Neo and +/+ P3 mice. Significance was determined using a 2-tailed Student's t-test. Average of N = 3 biological replicates; error bars \pm SD. (B) Cartilage from the distal humerus of Neo/Neo and +/+ samples stained with safranin O (orange) and hematoxylin (purple) revealed disrupted growth plates (asterisks) and pericellular regions (arrowheads), and an increase in GAG in the articulating surface (S) of Neo/Neo samples. Scale bars: Overview: 400 μ m, Surface: 100 μ m. (C) Staining for hyaluronic acid (HA) using hyaluronic acid binding protein (HABP; green) indicated a difference in HA expression in the epiphysis of developing cartilage. Articular surface indicated by yellow dashed line. Type II collagen (COL2A1; red) in the distal humeral epiphysis was increased in Neo/Neo samples compared to +/+ littermates. Nuclei were stained with DAPI (blue). Scale bar: 100 μ m. Images representative of N = 3 biological replicates.

3.3. Matrisome composition was disrupted in perlecan-deficient cartilage

To determine how overall ECM protein, or matrisome, composition was affected by perlecan knockdown, we used LC-MS/MS to analyze the distal humeri of E16.5 and P3 +/+, heterozygous (Neo/+), Neo/Neo mice. E16.5 captures the developmental period prior to PCM condensation (Xu et al., 2016b). Samples from both forelimbs were pooled and physically disrupted in a chaotropic buffer (4M GuHCl). Then proteins were extracted, digested into peptides and analyzed by LC-MS/MS (Fig. B.2). Between 59 and 74 matrisome components were identified in each sample (Fig. 3.3A; Table S1). The raw intensities of proteins within experimental groups were normalized using label-free quantification (LFQ) in MaxQuant to enable comparison of relative protein abundance as a function of development and perlecan knockdown (Cox et al., 2014). To summarize LC-MS/MS results, proteins were grouped into tissue compartments (matrisome, cytoskeletal, nuclear, membrane, and other proteins) defined by classifications from the Matrisome and Gene Ontology Projects following (Mi et al., 2018; Naba et al., 2012; Saleh et al., 2019). We observed an increase in the composition of matrisome and a decrease in nuclear and other proteins between E16.5 and

P3 independent of genotype. While not significantly different, the relative abundance of matrisome was higher in perlecan-deficient mice at P3 than that of *+/+* littermates ($p = 0.0868$; Fig. 3.3B). Importantly, perlecan protein (HSPG2) knockdown was confirmed (Fig. 3.3C), providing confidence that changes in ECM content can be resolved using our experimental workflow. Volcano plots were generated to visualize dysregulated proteins as a function of development and perlecan knockdown (Fig. B.3). Changes in protein abundance were more pronounced as a function of development between *+/+* E16.5 and P3 timepoints than between Neo/Neo and *+/+* cartilage at E16.5 or P3.

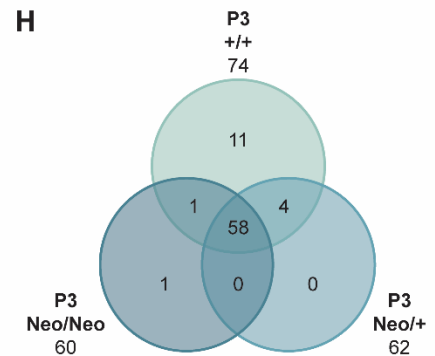
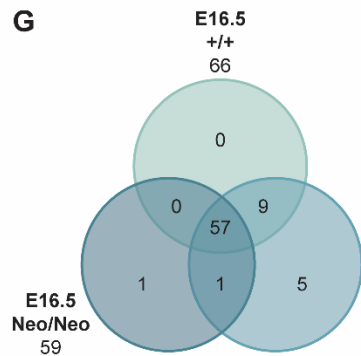
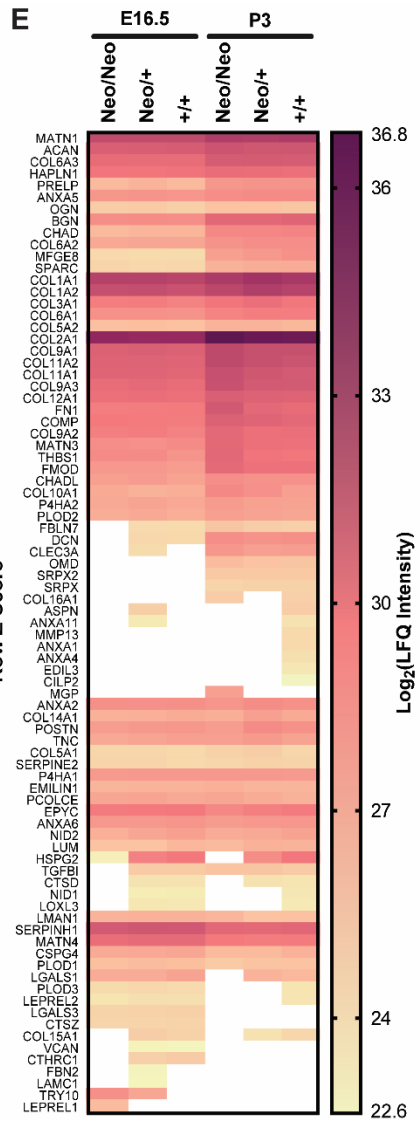
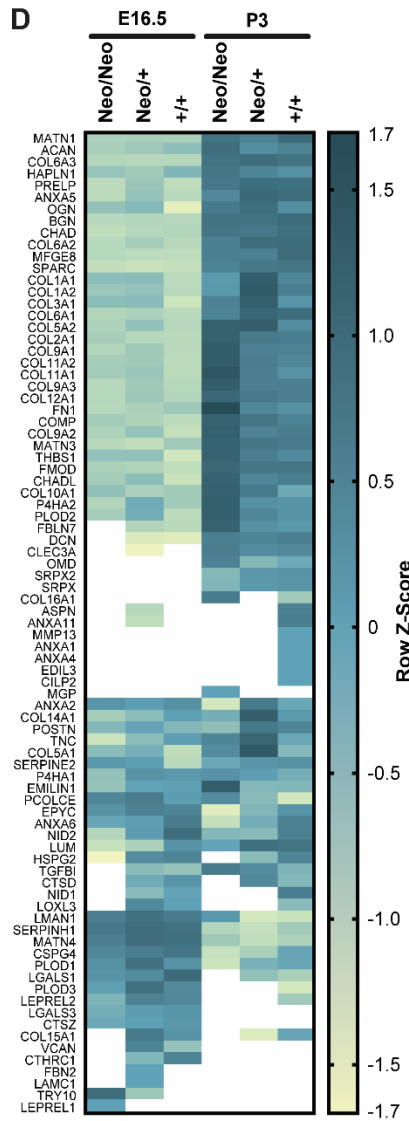
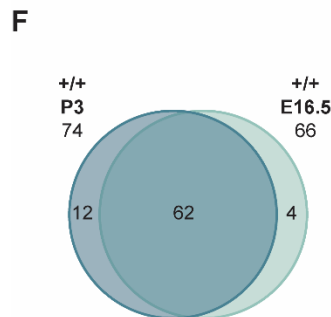
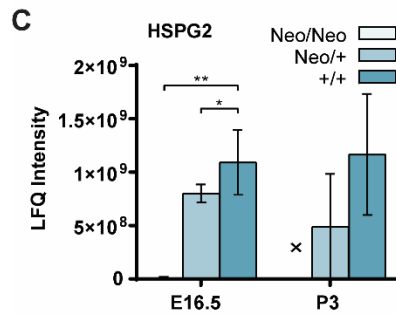
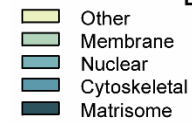
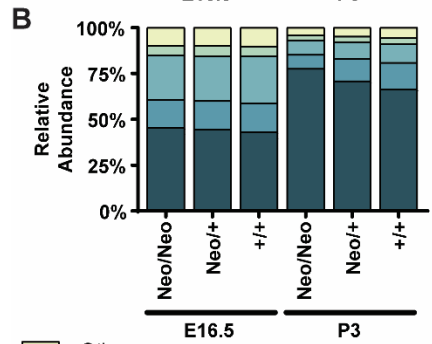
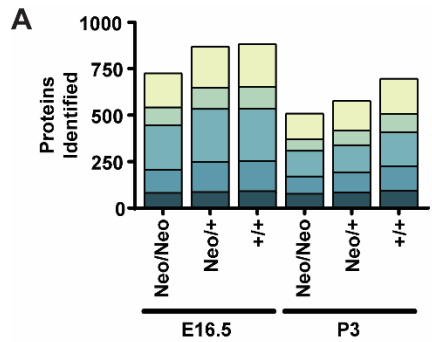
Between E16.5 and P3, there was a significant increase in the abundance of 27 matrisome components in *+/+* samples, including collagen types II, VI (COL6A1, A2, & A3), IX (COL9A1, A2, & A3), and XI (COL11A1 & A2), biglycan (BGN), cartilage oligomeric matrix protein (COMP), chondroadherin (CHAD), fibronectin (FN1), and matrilin-1 and -3 (MATN1 & 3) (Fig. 3.3D, E; Table S1). Significance was determined using a 2-tailed Student's t-test to analyze individual proteins. Additionally, type XVI collagen (COL16A1), EGF-like repeat and discoidin I-like domain-containing protein 3 (EDIL3), osteomodulin (OMD), sushi repeat-containing proteins (SRPX, SRPX2), and seven other matrisome components were uniquely identified in P3 *+/+* cartilage compared to E16.5 *+/+* (Fig. 3.3F; Table S1). Matrix proteins found only in E16.5 *+/+* samples when compared with P3 *+/+*, were collagen triple helix repeat-containing protein 1 (CTHRC1), cathepsin z (CTS2), galectin-3 (LGALS3), and versican core protein (VCAN) (Fig. 3.3F; Table S1). Chondroitin sulfate proteoglycan 4 (CSPG4), lectin mannose-binding 1 (LMAN1), serpin H1 (SERPINH1), matrilin-4 (MATN4), and lysyl hydroxylase 3 (PLOD3) were significantly more abundant in E16.5 *+/+* cartilage (Fig. 3.3D, E; Table S1).

Perlecan knockdown affected the relative abundance of matrisome components. Epiphycan (EPYC), lumican (LUM), and NID2 were significantly higher in *+/+* cartilage, consistent with HSPG2 (Fig. 3.3D, E; Table S1). Annexin A6 (ANXA6), CSPG4, and nidogen-1 (NID1) also trended similarly. Within E16.5 samples, only HSPG2 and NID2 were significantly higher in *+/+* compared to Neo/Neo littermates. Trypsin 10 (TRY10) abundance was significantly higher in Neo/Neo than Neo/+ cartilage and not present in E16.5 *+/+* samples (Table S1). Prolyl 3-hydroxylase 2 (LEPREL1) was the only matrisome component uniquely identified in E16.5 Neo/Neo cartilage (Fig. 3.3G). In contrast, perlecan deficiency led to more unique protein identifications and significant differences in protein abundance at P3. Eleven ECM proteins were

only observed in P3 +/+ cartilage, including asporin (ASPN), prolyl 3-hydroxylase 3 (LEPREL2), lysyl oxidase homolog 3 (LOXL3), PLOD3, and collagenase 3 (MMP13) (Fig. 3.3H; Table S1). P3 +/+ cartilage had significantly more EPYC (Fig. 3.3D, E; Table S1). Interestingly, a group of proteins was more abundant in P3 Neo/+ cartilage compared to the other genotypes. Annexin A2 (ANXA2), COL6A1, and LUM were significantly more abundant compared to Neo/Neo samples, and type V collagen (COL5A1 & A2) was significantly more abundant compared to +/+ samples (Table S1). Collagen types I (COL1A1 & A2), III (COL3A1), and XIV (COL14A1), periostin (POSTN), and tenascin-C (TNC), as well as five other proteins, were also highest in P3 Neo/+ cartilage. Since type I collagen is not typically described as being prevalent in hyaline cartilage, we immunostained for type I collagen and found strong expression on the articulating surface and positive staining within the epiphysis (Fig. B.4), consistent with a previous study that reported type I collagen synthesis in developing avian cartilage (Eyre et al., 1978).

Interestingly, many matrisome components were more abundant in the perlecan-deficient cartilage compared to +/+ littermates. P3 Neo/Neo cartilage had significantly more collagen types IX (COL9A1 & A2), COL11A1 & A2, COMP, fibromodulin (FMOD), FN1, LMAN1, MATN3, lysyl hydroxylase 2 (PLOD2), and thrombospondin-1 (THBS1). COL2A1, COL10A1, fibulin-7 (FBLN7), procollagen C-endopeptidase enhancer 1 (PCOLCE), and thirteen additional proteins were also more abundant in Neo/Neo cartilage (Fig. 3.3D, E; Table S1).

Fig. 3.3. Overview of the matrisome of developing murine cartilage. (A) Protein identification counts and (B) relative abundance of matrisome, cytoskeletal, nuclear, and membrane tissue compartments of the distal humerus as defined by the Matrisome and Gene Ontology Projects (Mi et al., 2018; Naba et al., 2012; Saleh et al., 2019). (C) The relative abundance of perlecan (HSPG2) decreased in Neo/+ and Neo/Neo cartilage. One-way ANOVA with post-hoc Tukey-adjusted comparison revealed a significant effect of genotype (* $p < 0.05$, ** $p < 0.01$) at E16.5. Error bars \pm SD. **X**: protein not identified. (D, E) Heat maps comparing cross-sample z-scores (D) and relative protein abundance (E) for the 83 matrisome proteins found in this study. Heat map for z-scores was sorted using biased clustering. White space indicates that protein was not identified. A protein was included if observed in at least 2 of $N = 3$ biological replicates. (F-H) Venn diagrams indicating the number of matrisome identified as a function of development (F) and as a function of perlecan knockdown at E16.5 (G) and P3 (H). Protein specific results, MaxQuant parameters, and analysis available in Supplemental Table S1.



3.4. Hydroxyproline and hydroxylysine modifications were not affected by perlecan knockdown

LC-MS/MS analysis indicated that the abundance of collagen and other matrisome components increased in P3 perlecan-deficient mice; however, this may be due to differences in the solubility of ECM in GuHCl as a function of genotype (Figs. 3.3, 3.4A). To validate our observation, we used a colorimetric assay to quantify hydroxyproline (Hyp) as a separate way to measure relative collagen abundance (Kesava Reddy and Enwemeka, 1996). Similar to the LC-MS/MS results, there was a significant increase in Hyp abundance with both age and perlecan knockdown (Fig. 3.4B).

In addition to collagen abundance, we considered the effect of perlecan knockdown on collagen fibril stability. Proline and lysine hydroxylation affect triple helix stability and fibril crosslinking, respectively (Berisio et al., 2004; Knott and Bailey, 1998). Our LC-MS/MS results indicated prolyl hydroxylases, the enzymes that hydroxylate prolines in the endoplasmic reticulum, were dysregulated; at P3, LEPREL2 was only identified in +/+ samples, while P4HA2 abundance increased with perlecan knockdown (Fig. 3.3D, E; Table S1). Furthermore, PLODs, which hydroxylate lysine in the endoplasmic reticulum, were also differentially regulated by perlecan knockdown. PLOD2 abundance significantly increased while PLOD1 decreased, and PLOD3 was not identified in P3 perlecan-deficient mice (Fig. 3.3D, E; Table S1).

To investigate the degree of proline and lysine hydroxylation, we included Hyp and hydroxylysine (Hyl) as variable modifications when the LC-MS/MS spectra were analyzed using MaxQuant. The percent of prolines hydroxylated was unchanged with perlecan knockdown (Fig. 3.4C), and the relative abundance of peptides with Hyp modifications mimicked the collagen trends (Fig. 3.4A, D). Similarly, perlecan knockdown did not significantly affect the level of lysine hydroxylation (Fig. 3.4E). The relative abundance of proteins with Hyl modifications had a trend analogous to total collagen and Hyp, increasing from E16.5 to P3, as well as with knockdown at P3 (Fig. 3.4A, D, F).

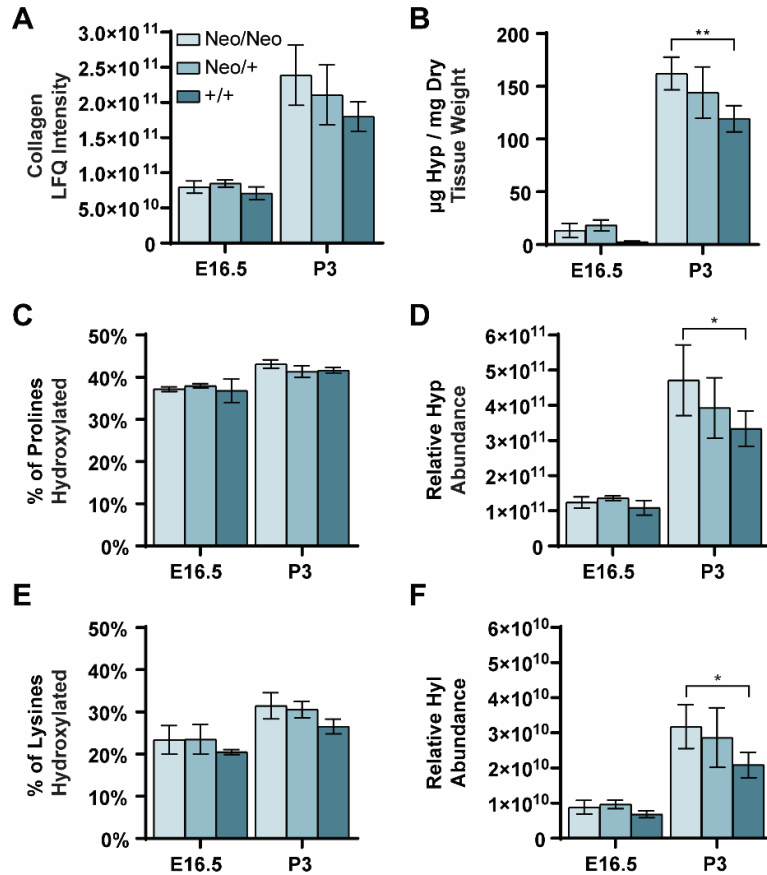


Fig. 3.4. Post-translational hydroxylation of collagens is not affected by perlecan knockdown. (A) LFQ intensity of collagen peptides increased as a function of age and knockdown at P3. (B) Hydroxyproline (Hyp) abundance measured using a colorimetric assay was consistent with LC-MS/MS results and revealed a significant increase in Hyp with perlecan knockdown at P3. (C) Perlecan knockdown did not affect the percentage of prolines hydroxylated. Percentage calculated from LFQ intensity. (D) The relative abundance of Hyp derived from LFQ intensity of all modified peptides significantly increased in perlecan-deficient P3 mice. (E) Perlecan knockdown did not affect the percentage of lysines hydroxylated. (F) Similar to Hyp, the relative abundance of hydroxylysine (Hyl) significantly increased with perlecan knockdown at P3. (A-F) The effect of age was significant for all comparisons ($p < 0.0001$). Significance determined by two-way ANOVA and Tukey-adjusted simple effects comparison ($p \geq 0.05$, * $p < 0.05$, ** $p < 0.01$). Results are the average of $N = 3$ biological replicates. Error bars \pm SD.

3.5. Perlecan knockdown did not affect collagen fibril diameter or volume fraction in developing cartilage

The addition of perlecan to *in vitro* culture increased the diameter of type I and type II collagen fibrils (Kvist et al., 2006); therefore, we hypothesized that the increase in collagen abundance observed in P3 Neo/Neo mice was due to an increase in density of smaller diameter fibrils. Transmission electron microscopy (TEM) of distal humeral cartilage revealed dark fibrils with the periodic banding structure of the fibril-forming collagens (Fig. B.5), which were randomly distributed in Neo/Neo and +/+ cartilage (Fig. 3.5A, B). These fibrils were presumed to be made up of primarily type II collagen and accessory molecules known to mediate fibril diameter (*e.g.*, collagens IX and XI) (Gelse et al., 2003). Fibrils in the center of the epiphysis appeared to be less organized than at the surface of the cartilage but were similar between Neo/Neo and +/+ littermates (Fig. 3.5C-F). There was no significant difference in fibril volume fraction between genotypes or cartilage regions (Fig. 3.5G). While the average diameter of fibrils in the center of the epiphysis was smaller than of those near the articulating surface for +/+ cartilage, it was not significantly smaller in perlecan-deficient mice (Fig. 3.5H).

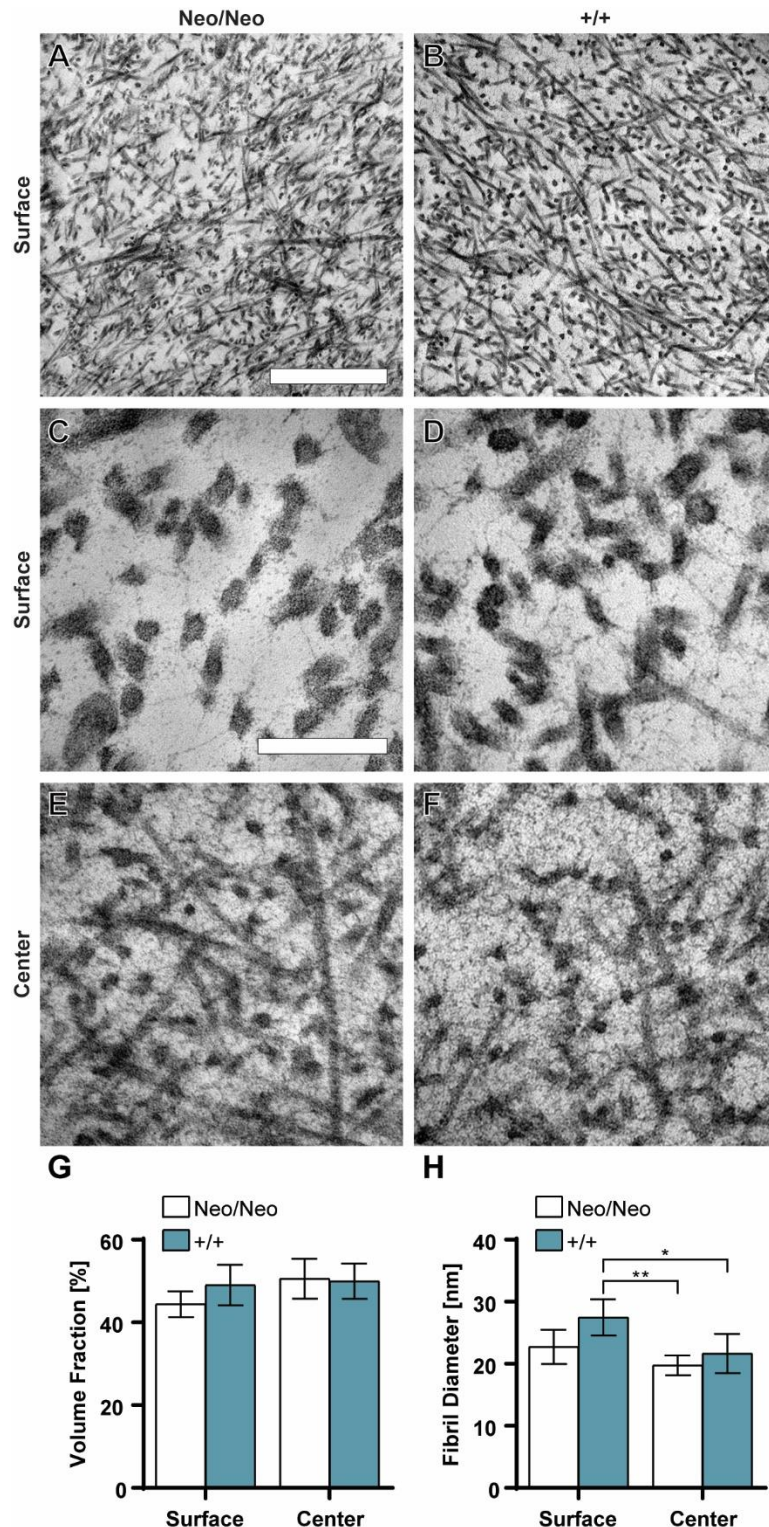


Fig. 3.5. Perlecan knockdown does not substantially affect epiphyseal fiber architecture. Representative TEM images of P3 cartilage from Neo/Neo mice (A, C, E) and +/+ littermates (B, D, F) at 30,000 \times (A, B) and 120,000 \times (C, D, E, F). Regions were selected near the articulating surface (Surface, A-D) or within the center of the epiphysis (Center, E, F) of the distal humerus. Scale bars: 750 nm and 200 nm, for (A, B) and (C, D, E, F), respectively. (G) Perlecan knockdown did not affect fibril volume fraction within the interstitial matrix. Results were averaged over three different images for $N = 4$ biological replicates. (H) Similarly, perlecan knockdown did not significantly affect fibril diameter; however, interstitial matrix within the center of the epiphysis had significantly smaller fibril diameters than near the surface ($p = 0.0066$). Significance determined by two-way ANOVA and post-hoc Tukey-adjusted comparison (* $p < 0.05$, ** $p < 0.01$). Results averaged over ≥ 27 randomly chosen, transversely oriented fibrils for $N = 4$ biological replicates. Error bars \pm SD.

3.6. Perlecan knockdown led to increased protein secretion *ex vivo*

Unable to visualize a major difference in bulk matrix ultrastructure, we hypothesized that the excess matrisome observed in P3 Neo/Neo cartilage was secreted into the interstitial space but not integrated into the overall ECM network. To quantify protein secretion, we incubated freshly harvested P3 distal humeri *ex vivo* for four days and collected and replaced the media every two days. During the incubation period, significantly more protein was secreted by Neo/Neo compared to +/+ cartilage explants ($p = 0.0033$; Fig. 3.6A).

There were no significant differences in the relative abundance of different tissue compartments between genotypes ($p > 0.9999$; Fig. 3.6B). Volcano plots were generated to visualize dysregulated proteins as a function of perlecan knockdown (Fig. B.6). Of the 109 matrisome components found, five were uniquely identified in Neo/Neo samples, including COL10A1 (Fig. 3.6C; Table S2). Conversely, type XVIII collagen (COL18A1), cathepsin B (CTSB), cathepsin L1 (CTSL), matrilin-2 (MATN2), matrix metalloproteinase-3 (MMP3), and four additional proteins were unique to +/+ samples (Fig. 3.6C; Table S2). HSPG2, BGN, collagen type XV (COL15A1), MATN1, and lactadherin (MFGE8) were significantly less abundant in the secretome of Neo/Neo mice as determined using a 2-tailed Student's t-test on individual proteins, whereas COL2A1 and NID2 were significantly more abundant in Neo/Neo mice (Fig. B.6; Table S2). Interestingly, alpha-2-macroglobulin-P (A2MP), a proteinase inhibitor (Lorent et al., 1994), was also increased in perlecan-deficient mice. COL11A1, LOXL3, MATN4, NID1, metalloproteinase inhibitor 1 (TIMP1), and TNC were also less abundant in the Neo/Neo secretome (Fig. B.6; Table S2).

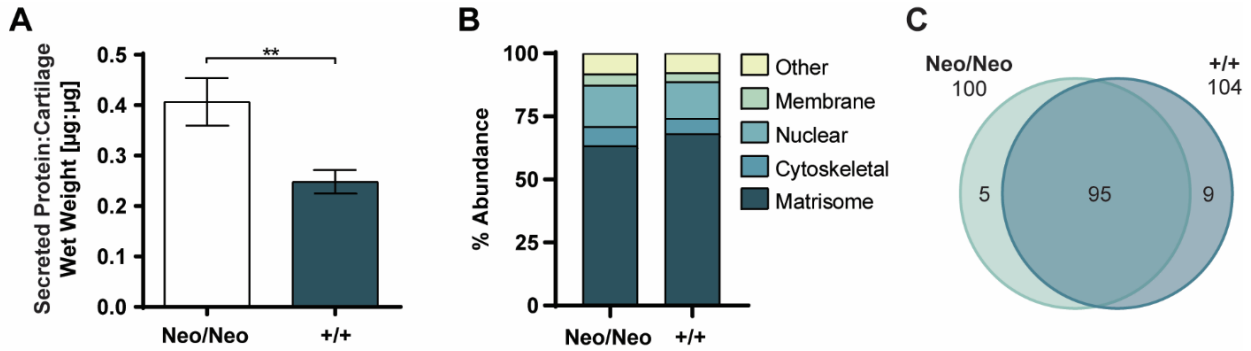


Fig. 3.6. Perlecan knockdown affects cartilage secretome. (A) Significantly more protein was secreted by P3 Neo/Neo cartilage explants as determined by normalizing the amount of protein in the supernatant by that in the explant. Results are reported as an average of $N = 3$ biological replicates. Significance was determined using a 2-tailed Student's t-test (** $p < 0.01$). Error bars \pm SD. (B) There were no significant differences in the compartments of proteins secreted by either genotype. (C) Venn diagram of matrisome identified in Neo/Neo and +/+ secretomes. Protein specific results, MaxQuant parameters, and analysis available in Table S2.

3.7. Chondrocyte volume increases in perlecan-deficient cartilage

Increased protein secretion in Neo/Neo explants may account for the abundant matrisome observed in cartilage LC-MS/MS results; however, the difference in matrisome composition may also be explained by an increased ECM to cell volume fraction in perlecan-deficient cartilage. To accurately measure how perlecan knockdown affected chondrocyte size and matrix volume fraction, we generated three-dimensional geometries based on the native physiology. Decellularized humeri from P3 Neo/Neo and +/+ mice were stained with wheat germ agglutinin (WGA), which labels a subset of proteoglycans in the remaining ECM. Confocal images acquired near the articulating surface of the distal humerus were processed in MATLAB to generate cellular and ECM geometries following Lycke et al., 2019 (Fig. 3.7A, B). The average volume of individual cells in perlecan-deficient cartilage was significantly higher than in +/+ littermates ($V_{\text{Neo/Neo}} = 326.02 \mu\text{m}^3 \pm 27.53$, $V_{+/+} = 183.16 \mu\text{m}^3 \pm 82.56$, average \pm SD, $p = 0.0467$, Fig. 3.7C). Nevertheless, cellular volume fraction (ϕ) calculated from the geometries trended toward less ECM in the Neo/Neo samples, but were not significantly different between Neo/Neo and +/+ samples ($\phi_{\text{Neo/Neo}} = 18.65\% \pm 0.75\%$, $\phi_{+/+} = 16.46\% \pm 1.30\%$, average \pm SD, $p = 0.0642$, Fig. 3.7D).

We previously demonstrated that age-related changes in cell-ECM geometry affected the strain experienced by the ECM when cartilage was modeled *in silico* (Lycke et al., 2019). To test if changes in chondrocyte volume due to perlecan knockdown affected the distribution of strain,

we combined the physiologically relevant geometries generated from confocal imaging with experimentally determined compressive moduli we previously measured using AFM (Table S3) (Xu et al., 2016b). The geometries were deformed by 5% unconfined compression using ANSYS (Fig. 3.7E), which is within the expected physiological range of 1-10% (Anderson and Johnstone, 2017; Liu et al., 2017). Simulations were run where the geometry and material properties matched the genotype, and then were mismatched, to see how both affected the resultant strain. ECM strain in Neo/Neo cartilage was significantly decreased compared to +/+ samples (Fig. 3.7F). Interestingly, chondrocytes experienced similar strains in response to applied compression even though the compressive moduli and individual cell volumes were significantly different as a function of perlecan knockdown (Fig. 3.7G).

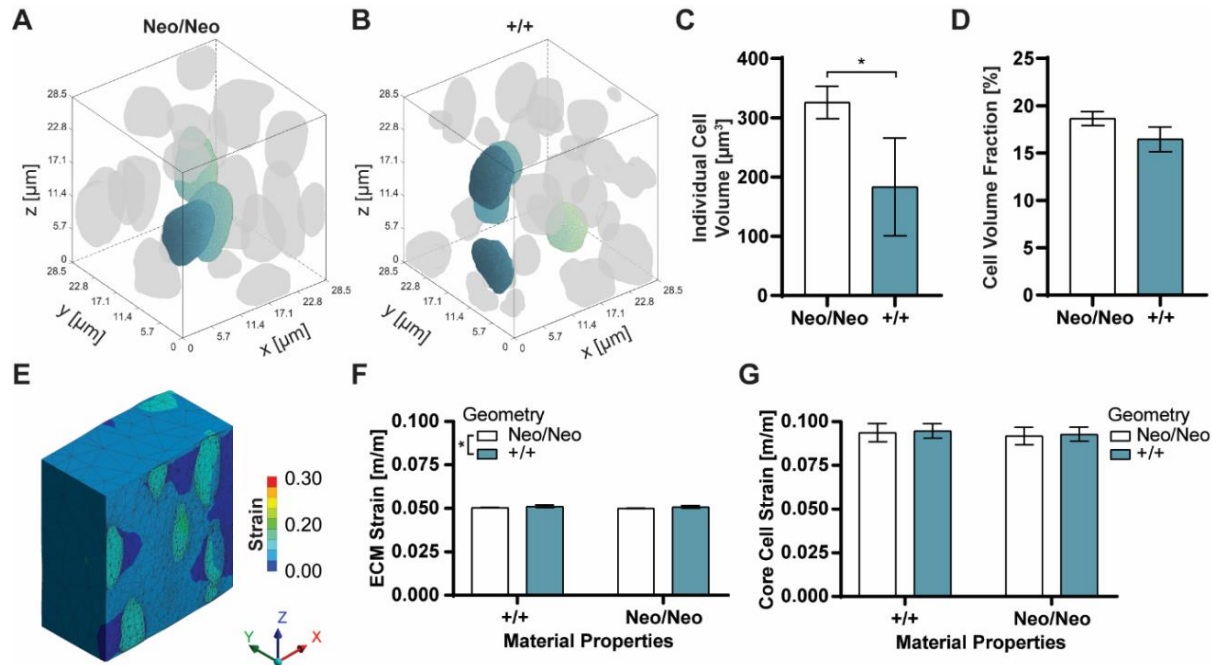


Fig. 3.7. Individual chondrocyte volume significantly increased due to perlecan knockdown. Representative cellular geometries from P3 Neo/Neo (A) and +/+ (B) humeri. Origin indicates the 3-4 cell layers within the articulating surface ($x = 0$). Cells within $1 \mu\text{m}$ of the boundary were not used for volume or strain calculations due to incomplete geometries and boundary edge effects. (C) The volume of individual chondrocytes from Neo/Neo mice were 78.0% larger than those from +/+ littermates. (D) The volume fraction occupied by cells was not significantly different as a function of genotype. (E) Finite element models based on the geometries were compressed 5% in the x -direction using ANSYS and revealed a slight, but significant decrease in ECM strain with the perlecan knockdown (F) while there was no difference in the strain experienced by the chondrocytes (G). ECM strain was (from left to right) 0.0504 ± 0.0001 , 0.0512 ± 0.0008 , 0.0500 ± 0.0002 , 0.0508 ± 0.0007 (F). Core cell strain was (from left to right) 0.0937 ± 0.0052 , 0.0946 ± 0.0041 , 0.0917 ± 0.0050 , 0.0927 ± 0.0040 (G) (Mean \pm SD). Three different areas from the articular surface were imaged, and results were averaged over $N = 3$ biological replicates. Significance was determined using a 2-tailed Student's t -test (C, D) or two-way ANOVA (F, G) (* $p < 0.05$). Error bars \pm SD.

4. DISCUSSION

The limited understanding regarding how cartilage forms during development hinders the design of early intervention methods to treat or prevent damaged cartilage. Additionally, the development of therapies for SJS and other cartilage diseases is inhibited by a lack of understanding of how perlecan deficiency affects the functionality of cartilage and leads to osteoarthritis. Although perlecan has been implicated in chondrogenic differentiation (French et al., 1999), cell-matrix mechanotransduction (Guilak et al., 2006; Vincent et al., 2007), and chondrocyte mechanical protection (Wilusz et al., 2012), the effect of perlecan deficiency on the overall organization and composition of the matrisome of developing cartilage has not been explored. Elucidating these effects will provide more insight into the role of perlecan on healthy cartilage development, as well as the progression of SJS and other chondrodysplasias.

4.1. Murine cartilage matrisome significantly changes during development

Proteomic analysis of developing cartilage revealed significant changes in protein expression during ECM remodeling within the epiphyses of E16.5 and P3 +/+ mice (Fig. 3.3; Table S1). Consistent with previous findings, matrisome components identified in E16.5 and P3 cartilage were categorized primarily as *collagen-containing extracellular matrix* (GO:0062023) (Wilson et al., 2012). Of the 78 matrisome identified in +/+ samples, 48 were differentially expressed or uniquely identified between timepoints. ECM identified at E16.5 reflected components known to be found during early matrix biosynthesis and organization (*e.g.*, LGALS3 and SERPINH1) (Boeuf et al., 2008; Iacobini et al., 2017). In contrast, the P3 matrisome was enriched in proteins related to ECM maturation and collagen fibril accessory proteins including COL9A3, COL11A1 & 2, and decorin (DCN) (Blaschke et al., 2000; Heinegård et al., 2015). Chondrocyte differentiation markers, COMP and CHAD, also emerged at P3, which correlate with chondrocyte maturation and progression towards ossification (Ishida et al., 2013; Tillgren et al., 2015).

4.2. Perlecan knockdown decreases abundance of PCM proteins

Comparison of matrisome expression between cartilage from perlecan-deficient and healthy littermates revealed many differences in ECM composition. We observed reduced NID2 immunofluorescence in the PCM and smaller pericellular regions stained with safranin O in perlecan-deficient P3 cartilage (Fig. 3.1B, 3.2B). Furthermore, LC-MS/MS indicated NID2, NID1, and COL15A1 were less abundant due to perlecan knockdown (Fig. 3.3D, E). These proteins are binding partners of perlecan, share similar protein domains, and colocalize in the PCM (Farach-Carson et al., 2014; Hopf et al., 1999). Analysis of the secretome of cartilage explants revealed decreased secretion of NID1 and COL15A1 with the knockdown, whereas NID2 was increased (Table S2). The absence of perlecan as a binding partner, combined with the known compensatory expression of nidogens (Bader et al., 2005; Miosge et al., 2002), may explain the excess NID2 secreted by Neo/Neo cartilage *in vitro*. We postulate that perlecan knockdown leads to the reduction of NID1 synthesis, resulting in an increase in NID2 synthesis. Since there is minimal perlecan in Neo/Neo cartilage, NID2 was not strongly bound to the PCM and released into the media. Notably, NID1, NID2, and COL15A1 were also significantly less abundant in the proteome of the residual cartilage after *ex vivo* incubation (Table S2), indicating that NID2 is not able to incorporate into the PCM. These results support previous observations that perlecan knockdown disrupted PCM formation during cartilage development (Rodgers et al., 2007). PCM composition and mechanics have been reported to play critical roles in protecting chondrocytes from mechanical loading (Guilak et al., 2006; Wilusz et al., 2012), and disruption may lead to changes in bulk matrix composition and integrity, contributing to the disease progression observed in SJS patients.

4.3. Perlecan regulates endochondral ossification during cartilage development

COL10A1 immunostaining was increased in Neo/Neo epiphyses (Fig. 3.1C). Previous reports that investigated perlecan null mice indicated no change in type X collagen expression in E15.5 and E18.5 cartilage (Costell et al., 1999; Ishijima et al., 2012), whereas we found little difference in abundance at E16.5. Innate differences in between the perlecan deficient and null models may account for this inconsistency, as well as our observation that there was no significant change in the matrix ultrastructure of perlecan deficient mice, while the collagen network was

disrupted in perlecan null mice (Costell et al., 1999). Our LC-MS/MS results also revealed that COL10A1 and OMD were increased in abundance in perlecan-deficient cartilage by P3 (Fig. 3.3D, E). Hypertrophic chondrocytes express COL10A1 during endochondral ossification (Long and Linsenmayer, 1998), and OMD is known to suppress cartilage matrix formation prior to ossification (Tashima et al., 2015). In addition, chondrocyte volume increased due to perlecan knockdown (Fig. 3.7C), and COL10A1 was only secreted by Neo/Neo samples (Table S2). Conversely, the secretome of +/+ cartilage uniquely contained matrix gla protein (MGP, Table S2) known to inhibit cartilage ossification (Newman et al., 2001). The differences in these markers supports the observation that ectopic ossification occurs in Neo/Neo cartilage (Arikawa-Hirasawa et al., 1999) and likely leads to the premature growth plate closure and shortened long bones observed in SJS patients (Arikawa-Hirasawa et al., 2001).

4.4. Matrisome compensation in perlecan-deficient cartilage

While we hypothesized that perlecan knockdown would decrease the abundance of PCM proteins, we did not expect to find an increase in bulk matrisome components (*e.g.*, COL2A1, COMP, and FN1) (Fig. 3.3D, E). Protein solubility is a major factor that influences the proteomic analysis of ECM-rich tissues, and some enzymes associated with collagen crosslinking were dysregulated due to perlecan knockdown (*e.g.*, PLOD1, 2, & 3, LEPREL2; Fig. 3.3D, E). However, the greater matrisome abundance did not appear to be caused by an increase in extractability. Overall Hyp abundance, measured using an assay with stronger extraction conditions than for LC-MS/MS, was also increased in perlecan knockdown cartilage, indicating the increase in bulk matrix in Neo/Neo mice was not an artifact of differences in solubility (Fig. 3.4A). Hyp and Hyl modification levels, indicative of collagen triple helix stability and fibril crosslinking, were not affected by perlecan knockdown (Fig. 3.5C, E). Additionally, immunofluorescent staining revealed an increase in type II collagen in Neo/Neo cartilage, consistent with the proteome and secretome results (Figs. 3.2C, 3.3D, E; Table S1).

It is counterintuitive that perlecan deficiency will lead to an increase in type II collagen and other bulk matrisome abundance, although elevated mRNA levels of COL2A1, MATN3, and COMP were previously reported in perlecan-null embryos (Costell et al., 1999). The spatio-temporal localization of perlecan during healthy development may provide an explanation for the increased matrisome abundance that emerges with perlecan knockdown. Perlecan is ubiquitously

expressed in the cartilage template at E16.5 in WT mice (Xu et al., 2016b). While there were few differences in the overall matrisome at E16.5, the effects of perlecan deficiency may take time to manifest within the tissue. By P3, perlecan is restricted to the PCM in healthy cartilage, and functional perlecan is not available in the P3 Neo/Neo cartilage to orchestrate the assembly of the bulk matrix. If the chondrocytes sense incorrect matrix assembly, due to the absence of a PCM that is thought to protect from mechanical loading and mediate growth factor signaling (Guilak et al., 2006; Vincent et al., 2007), bulk matrix synthesis may be increased to counteract the absence of the PCM. However, the developing ECM network in perlecan-deficient cartilage is unable to incorporate the excess proteins for reasons that currently remain unclear.

4.5. Excess matrix is not incorporated into the ECM network of perlecan knockdown cartilage

Collagen fibril assembly *in vitro* is accelerated in the presence of chondroitin sulfate enriched perlecan fragments (Kvist et al., 2006), indicating perlecan deficiency would lead to disrupted matrix ultrastructure. In addition, when perlecan was knocked out *in vivo*, collagen fibrils in the growth plate appeared shorter (Costell et al., 1999); however, we observed no difference in collagen fibril volume fraction and fibril diameter between the epiphyses of P3 Neo/Neo and +/+ littermates (Fig. 3.5). These discrepancies may be attributed to differences in model systems and locations within developing cartilage. Additionally, cellular and matrix geometries generated from WGA-stained decellularized cartilage revealed no significant difference in volume fraction as a function of perlecan knockdown (Fig. 3.7D).

Since neither ultrastructure nor matrix volume fraction could account for the increased matrisome abundance in Neo/Neo cartilage, we then tested if the excess ECM was not incorporating into the developing network. Incubation of explants *in vitro* confirmed that more protein was released from perlecan-deficient cartilage, which may explain why there was no significant difference in the fibril diameter or volume fraction (Figs. 3.5, 3.6A). Alternatively, degradation may be affected, leaving excess matrisome to be secreted but not broken down. Proteomic analysis of secreted proteins revealed that CTSB, CTSL, and MMP3 were exclusively identified in the +/+ secretome. Heparan sulfate GAGs bound to perlecan are known to sequester cathepsins and provide the acidic environment necessary to maintain endopeptidase activity (Almeida et al., 2001). These collagen degradation enzymes may fine-tune ECM assembly in +/+

cartilage (Flanagan-Steet et al., 2018; Turk et al., 2012), and reduced enzyme abundance and activity could explain the increase in matrix proteins in Neo/Neo cartilage (Fig. 3.3D, E). In addition, the proteinase inhibitor A2MP was significantly more abundant in Neo/Neo secretome (Lorent et al., 1994) (Table S2), providing further evidence that matrix turnover is affected by perlecan knockdown.

Although there was no significant difference in the level of post-translational collagen hydroxylation (Fig. 3.4), crosslinking may be affected by perlecan knockdown. Specifically, lysyl oxidase-like proteins (LOXL2 & 3) were less abundant in the perlecan-deficient secretome (Table S2), whereas LOXL3 was uniquely identified in P3 *+/+* cartilage (Table S1). Decreased LOXL3, combined with an increase in COL2A1 secretion (Table S2), indicates that type II collagen trimers secreted by chondrocytes were not stably incorporated into the bulk matrix of perlecan-deficient cartilage.

4.6. Haploinsufficiency of perlecan alters developing cartilage matrix

Interestingly, some ECM proteins were elevated in Neo/+ but not Neo/Neo mice. These proteins included COL1A1 & A2, COL3A1, COL5A1 & A2, TNC, and POSTN. The abundance of these collagens is known to increase early in bone fracture callus formation (Bland et al., 1999; Miedel et al., 2015), and TNC and POSTN are associated with the fibrotic response to injury (Chijimatsu et al., 2015; Okamura et al., 2010). Perlecan haploinsufficiency may be interpreted as damaged tissue by chondrocytes, leading to a pseudo-fibrotic response. However, the lack of a further increase of these ECM proteins in Neo/Neo mice suggests that the effect of perlecan is not linearly correlated with the overall concentration. Further work is necessary to confirm that a mild decrease in perlecan abundance evokes a fibrotic response in cartilage.

4.7. Perlecan supports articular cartilage mechanics by regulating GAG deposition

It was previously shown that perlecan knockdown leads to decreased GAG abundance in the developing growth plate of long bones (Arikawa-Hirasawa et al., 1999; Costell et al., 1999; Ishijima et al., 2012; Rodgers et al., 2007). In contrast, a recent report showed that GAG deposition was increased in the vertebral growth plates of heparan sulfate-deficient, *Hspg2* exon 3-null mice, resulting in accelerated chondrocyte hypertrophy and abnormal bone formation (Shu et al., 2019).

Our study of the developing epiphysis also revealed an increase in GAGs with perlecan knockdown. While a biochemical assay for sGAGs indicated no significant difference between genotypes, safranin O staining showed an overall increase in GAG deposition near the articulating surface of P3 perlecan-deficient mice, which may be attributed to differential expression of HA (Fig. 3.2). AFM studies of the bulk matrix in hyaluronidase-treated bovine cartilage (Xu et al., 2016a) and heparinase-treated porcine cartilage (Wilusz et al., 2012) showed an increase in compressive modulus when GAG networks were broken down. Interestingly, we previously demonstrated that there was a decrease in compressive moduli of bulk matrix and chondrocytes at the articulating surface of *Hspg2*^{C1532Y-Neo} mice compared to wildtype littermates (Xu et al., 2016b). Together, the AFM, safranin O, and HABP results indicate that perlecan influences GAG deposition in developing articular cartilage, ultimately decreasing the compressive modulus of the bulk matrix.

In addition to altered mechanical properties, we observed an increase in cell size near the articulating surface (Fig. 3.7A, B). The chondrocytes in Neo/Neo cartilage may be generally larger than those of +/+ littermates, but increased size is also indicative of hypertrophy. Indeed, perlecan-deficient adult mice have a reduced amount of articular cartilage (Rodgers et al., 2007). The expansion of the hypertrophic zone, combined with the decreased compressive modulus near the articulating surface of Neo/Neo samples, could impact the ability of cartilage to withstand cyclic loading and lead to the early damage and onset of osteoarthritis observed in perlecan-deficient mice and SJS patients (Arikawa-Hirasawa et al., 2001; Rodgers et al., 2007).

4.8. Perlecan knockdown affects chondrocyte geometry and mechanics

Although chondrocyte volume was significantly larger in Neo/Neo cartilage (Fig. 3.7C), the similarity in cellular volume fraction compared with +/+ tissue indicated that the increase in matrix volume was not due to changes in cell-matrix volumetric distributions. Interestingly, the volume fractions for the P3 +/+ cartilage were the same as in our previous study that used a different strain of mice (Lycke et al., 2019), demonstrating the repeatability of this method for generating physiologically relevant geometries.

In addition to measuring cell volume, the three-dimensional geometries enabled us to simulate compressive loading and examine the biomechanical response of perlecan-deficient and healthy ECM and chondrocytes. The changes in geometry primarily contributed to the decreased

strain experienced by the ECM ($p = 0.0412$), and not the change in material properties ($p = 0.2801$) as determined by two-way ANOVA (Fig. 3.7G). Notably, cellular strain was not different between Neo/Neo and +/+ tissues, and neither geometry ($p = 0.7146$) nor material properties ($p = 0.4902$) significantly contributed (Fig. 3.7F). This may indicate the chondrocytes are adapting to the lack of perlecan by reorganizing the ECM to maintain constant average strain within the cells. Cellular strain was amplified ~1.84-fold compared to ECM strain, similar to previous reports (Cao et al., 2009; Cao et al., 2011; Guo et al., 2014; Lycke et al., 2019). Overall, these results suggest that chondrocytes increase their size and adjust their metabolism in the absence of perlecan to maintain constant strain.

In summary, we report how the proteomic composition of developing murine cartilage significantly changes as a function of development and perlecan knockdown. Our analysis provides additional support that perlecan plays important roles in the formation of a functional PCM, restriction of GAGs from articular cartilage, and inhibition of endochondral ossification. Furthermore, the increase in GAGs may explain why we previously observed that the compressive modulus of articular cartilage decreases in perlecan-deficient mice (Xu et al., 2016b). These results suggest that chondrocytes are compensating for the lack of perlecan by secreting excess ECM to counteract decreased matrix integrity; however, the excess ECM is not able to incorporate into the network. SJS disease progression and the events that lead to the osteoarthritic phenotype are becoming more evident, but the underlying mechanisms by which perlecan delays hypertrophy in articular cartilage remains unclear. Future studies that directly quantify matrix crosslinking, such as biochemical assays or reverse-phase high-performance liquid-chromatography, may better elucidate the effect of perlecan knockdown on fibrillar matrix integrity and ultimately the functionality of cartilage.

APPENDIX A. ADDITIONAL INFORMATION

A.1. Supplemental information

Fig. B.1 – Altered Nidogen-2 and type X collagen expression in perlecan-deficient mice.	45
Fig. B.2 – Workflow for proteomic analysis of developing murine cartilage	47
Fig. B.3 – Cartilage composition significantly varies as a function of age and genotype...	48
Fig. B.4 – Type I collagen expression in the developing epiphysis	49
Fig. B.5 – Collagen banding patterns in developing cartilage	49
Fig. B.6 – Cartilage secretome composition varies as a function of genotype	50
Table S1 – Cartilage LC-MS/MS Results	See Attached
Table S2 – Secretome and Residual Cartilage LC-MS/MS Results	See Attached
Table S3 – Compressive Moduli of Cells and ECM	See Attached

A.2. Acknowledgments for this work

I would like to thank Victoria Hedrick for her consultation and LC-MS/MS operation at the Purdue Proteomics Core. Additionally, I acknowledge Wenbin Zhu at the Purdue Statistical Consulting Service and Robert Seiler at the Purdue Life Science Microscopy Facility for their contributions and consultation.

A.3. Direct contributions for this work

Alexander R. Ocken	Conceptualization, Methodology, Validation, Formal Analysis, Investigation, Writing – original draft, Writing – review and editing, Visualization, and Funding acquisition.
Madeline M. Ku	Validation, Investigation, Writing – original draft, Writing – review and editing, and Visualization.
Dr. Tamara Kinzer-Ursem	Conceptualization, Writing – review and editing, and Supervision.
Dr. Sarah Calve	Conceptualization, Methodology, Validation, Formal Analysis, Investigation, Writing – original draft, Writing – review and editing, Visualization, Supervision, and Funding acquisition.

A.4. Funding for this work

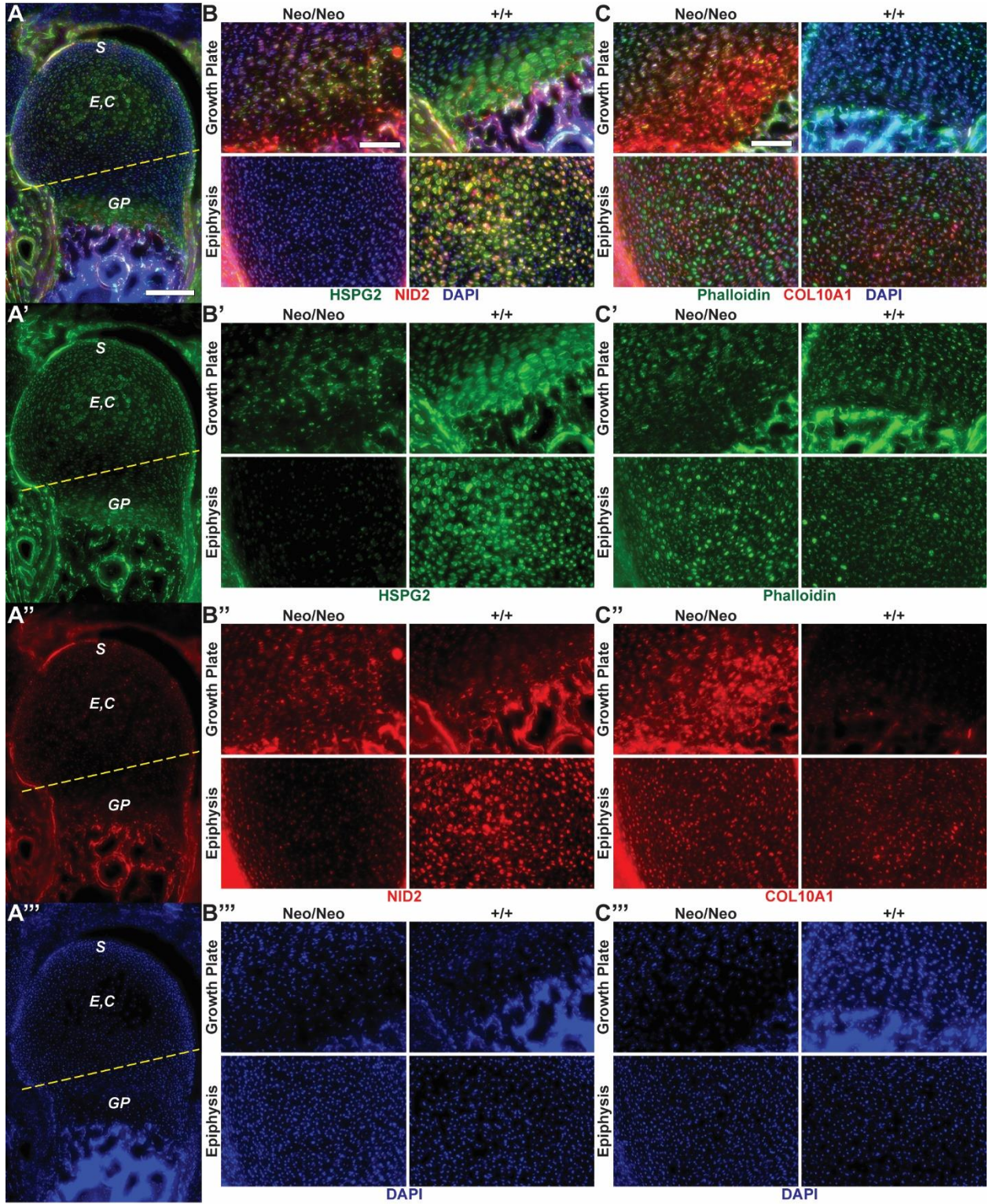
This work was supported by the National Institutes of Health [R01 AR071359 and DP2 AT009833 to S.C.] and the Charles C. Chappelle Fellowship [to A.R.O.]

A.5. Data availability

The mass spectrometry proteomics data have been deposited in the MassIVE repository under the DOIs: 10.25345/C5BT0W (Cartilage) and 10.25345/C5Z66J (Secretome) (Ocken et al., 2019a; Ocken et al., 2019b).

APPENDIX B. SUPPLEMENTAL FIGURES

Fig. B.1. Altered Nidogen-2 and type X collagen expression in perlecan-deficient mice. P3 cartilage from the distal humerus was immunofluorescent stained. (A) Perlecan (green) stained in +/+ cartilage. Dissection plane for biochemical and LC-MS/MS experiments indicated by yellow dashed line. *S*: articular surface, *E*: epiphysis, *C*: center, *GP*: growth plate. (B) Perlecan (HSPG2; green) and nidogen-2 (NID2; red) staining. (C) Type X collagen (COL10A1; red) and phalloidin staining (green). Nuclei were stained with DAPI (blue). Scale bars: (A) 200 μm , (B, C) 100 μm . (: green channel, ': red channel, ': blue channel). Images representative of N = 3 biological replicates.



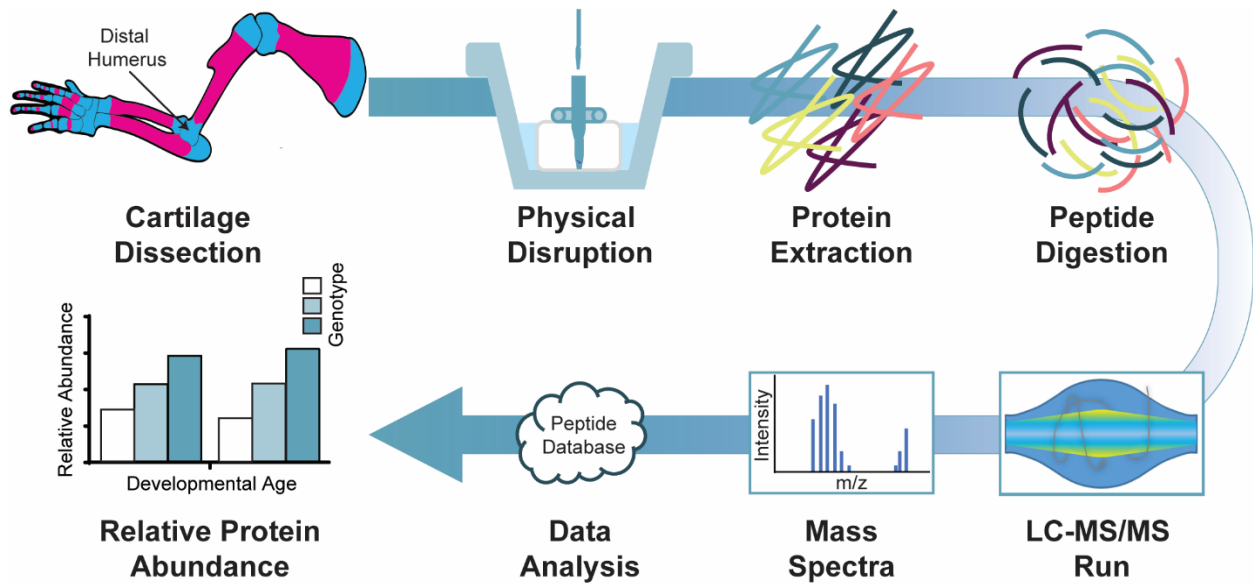


Fig B.2. Workflow for proteomic analysis of developing murine cartilage. Cartilage was dissected from the distal humerus (dissected region indicated in Fig 3.1A) and physically disrupted in 4M GuHCl. Then protein was extracted and digested into peptides using trypsin. Mass spectra were obtained by LC-MS/MS and analyzed *in silico* using MaxQuant to compare relative protein abundance as a function of development and perlecan knockdown.

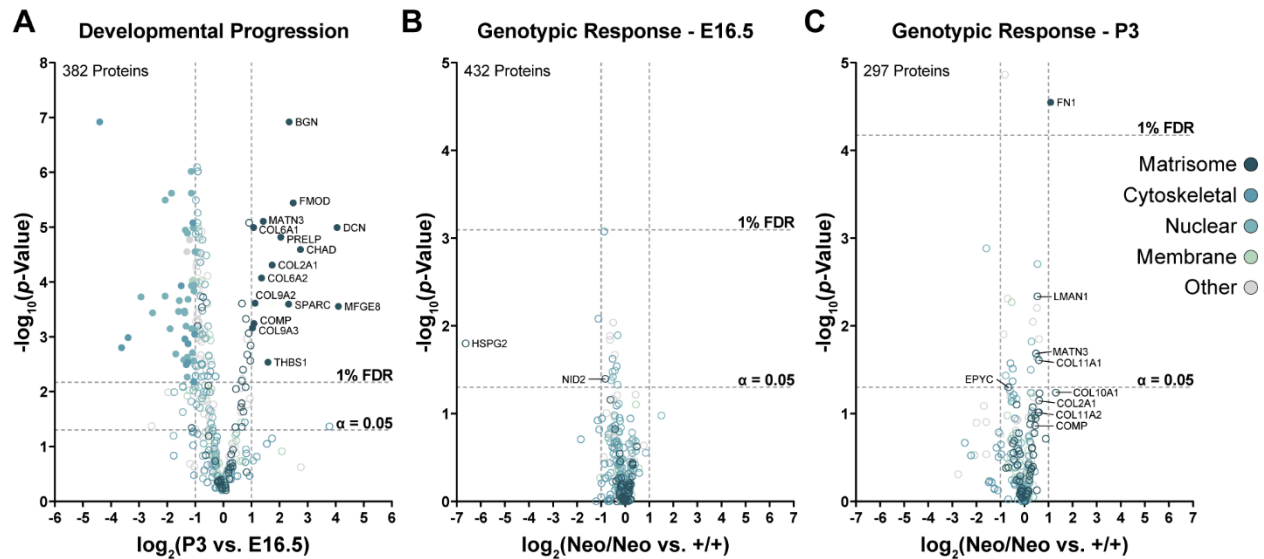


Fig B.3. Cartilage composition significantly varies as a function of age and genotype. (A) All matrisome components that were significantly different between the two time points were upregulated at P3. Volcano plot showing fold change in relative protein abundance between E16.5 and P3 for +/+ cartilage based on p -values calculated using one-way ANOVA of the \log_2 transformed LFQ intensity for each protein. (B, C) Volcano plots showing fold change in relative protein abundance between Neo/Neo mice and +/+ littermates at E16.5 (B) and P3 (C). Significance determined by two-way ANOVA and Tukey-adjusted simple effects comparison of \log_2 transformed LFQ intensity for each protein. Only proteins that were identified in at least two biological replicates ($N = 3$) were included, which totaled 382, 432, and 297 proteins for A, B, and C, respectively. Vertical grey lines represent a 2-fold difference in abundance, and horizontal grey lines reflect threshold for proteins with significantly different abundance calculated using a 1% FDR and $\alpha = 0.05$ threshold. Filled circles indicate proteins that are more than 2-fold different between groups and are statistically significant based on the 1% FDR.

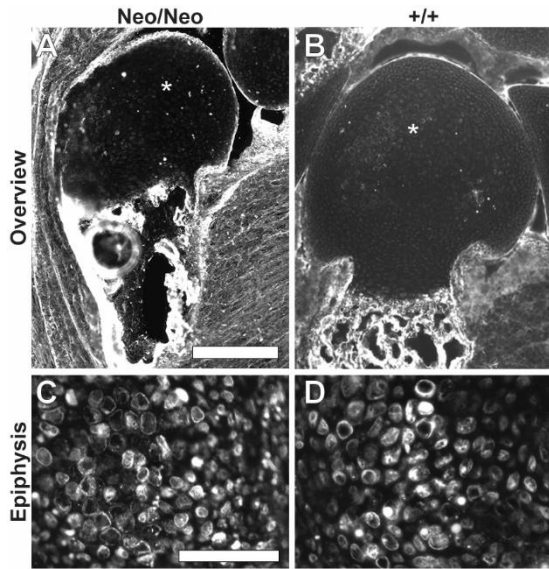


Fig B.4. Type I collagen expression in the developing epiphysis. (A, B) Type I collagen staining was strong in the developing bone, articulating surface, and epiphysis of the developing cartilage in the distal humerus at P3. Scale bar: 300 μ m. (C, D) Contrast-enhanced, magnified image from A and B (asterisks) indicates that type I collagen was also found within the developing epiphysis, consistent with the LC-MS/MS results (Fig. 3.3, Table S1). Scale bar: 100 μ m.

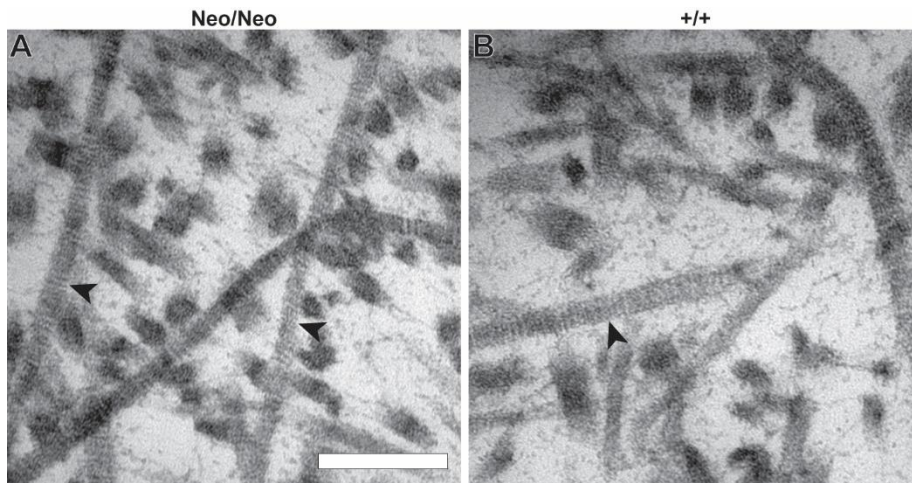


Fig B.5. Collagen banding patterns in developing cartilage. D-banding periodicity was observed in fibrils visualized in 120,000 \times TEM images of Neo/Neo (A) and +/+ (B) epiphyses of murine P3 cartilage (black arrowheads). Scale bar: 200 nm.

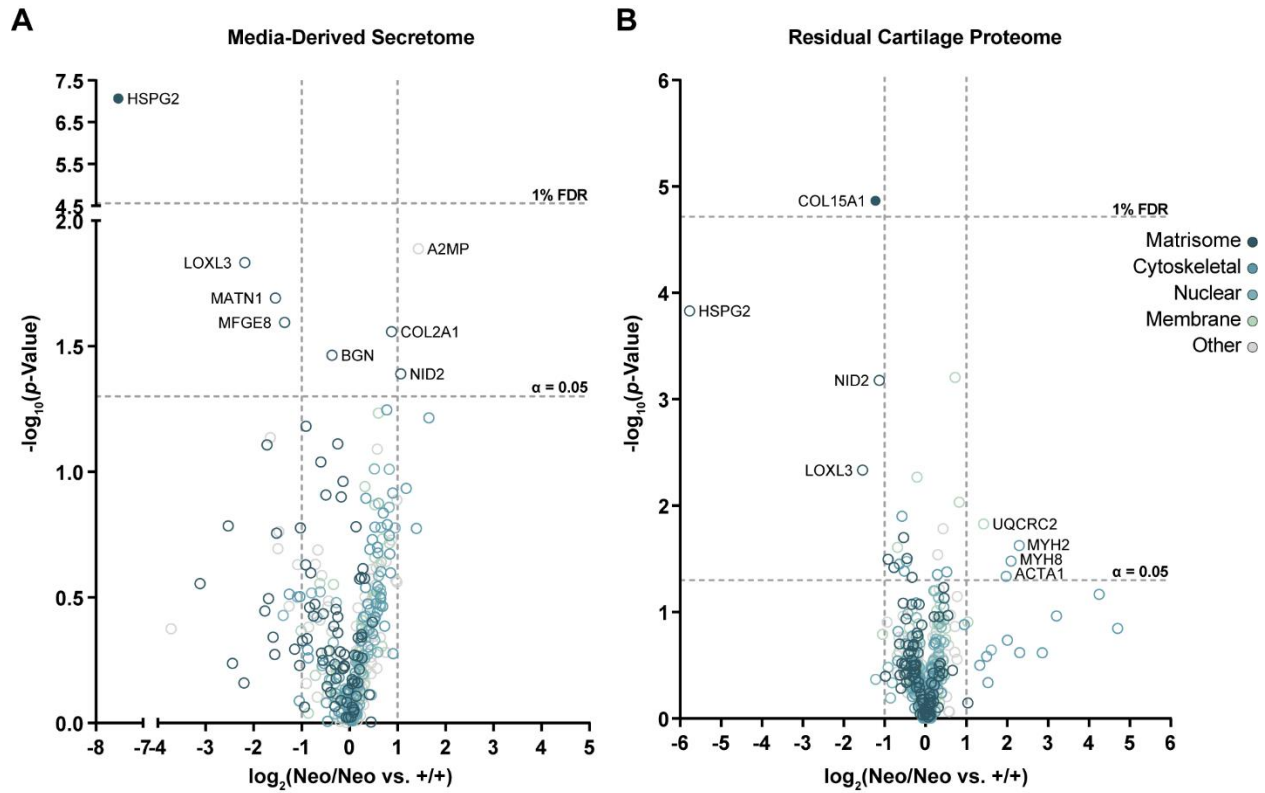


Fig B.6. Cartilage secretome composition varies as a function of genotype. (A, B) Volcano plots showing fold change in relative protein abundance secreted (A) and remaining within residual cartilage (B) between Neo/Neo mice and +/+ littermates at P3. Only proteins that were identified in at least two biological replicates ($N = 3$) are plotted, which totaled 362 (A) and 521 (B) proteins. Vertical grey lines represent a 2-fold difference in abundance, and horizontal grey lines reflect threshold for proteins with significantly different abundance calculated using a 1% FDR and $\alpha = 0.05$ threshold. Filled circles indicate proteins that are more than 2-fold different between groups and are statistically significant. Significance determined by 2-tailed Student's t-test of \log_2 transformed normalized values derived from LFQ intensity for each protein.

REFERENCES

- Almeida, P. C., Nantes, I. L., Chagas, J. R., Rizzi, C. C. A., Faljoni-Alario, A., Carmona, E., Juliano, L., Nader, H. B. and Tersariol, I. L. S.** (2001). Cathepsin B activity regulation. Heparin-like glycosaminoglycans protect human cathepsin B from alkaline pH-induced inactivation. *J. Biol. Chem.* **276**, 944–951. doi:10.1074/jbc.M003820200
- Anderson, D. E. and Johnstone, B.** (2017). Dynamic mechanical compression of chondrocytes for tissue engineering: A critical review. *Front. Bioeng. Biotechnol.* **5**, 76. doi:10.3389/fbioe.2017.00076
- Arikawa-Hirasawa, E., Watanabe, H., Takami, H., Hassell, J. R. and Yamada, Y.** (1999). Perlecan is essential for cartilage and cephalic development. *Nat. Genet.* **23**, 354–358. doi:10.1038/15537
- Arikawa-Hirasawa, E., Wilcox, W. R., Le, A. H., Silverman, N., Govindraj, P., Hassell, J. R. and Yamada, Y.** (2001). Dyssegmental dysplasia, Silverman-Handmaker type, is caused by functional null mutations of the perlecan gene. *Nat. Genet.* **27**, 431–434. doi:10.1038/86941
- Bader, B. L., Smyth, N., Nedbal, S., Miosge, N., Baranowsky, A., Mokkapati, S., Murshed, M. and Nischt, R.** (2005). Compound genetic ablation of nidogen 1 and 2 causes basement membrane defects and perinatal lethality in mice. *Mol. Cell. Biol.* **25**, 6846–6856. doi:10.1128/MCB.25.15.6846-6856.2005
- Benjamini, Y., Krieger, A. M. and Yekutieli, D.** (2006). Adaptive linear step-up procedures that control the false discovery rate. *Biometrika* **93**, 491–507. doi:10.1093/biomet/93.3.491
- Berisio, R., Granata, V., Vitagliano, L. and Zagari, A.** (2004). Imino acids and collagen triple helix stability: characterization of collagen-like polypeptides containing hyp-hyp-gly sequence repeats. *J. Am. Chem. Soc.* **126**, 11402–11403. doi:10.1021/ja047069h
- Bland, Y. S., Critchlow, M. A. and Ashhurst, D. E.** (1999). The expression of the fibrillar collagen genes during fracture healing: Heterogeneity of the matrices and differentiation of the osteoprogenitor cells. *Histochem. J.* **31**, 797–809. doi:10.1023/A:1003954104290
- Blaschke, U. K., Eikenberry, E. F., Hulmes, D. J. S., Galla, H.-J. and Bruckner, P.** (2000). Collagen XI nucleates self-assembly and limits lateral growth of cartilage fibrils. *J. Biol. Chem.* **275**, 10370–10378. doi:10.1074/jbc.275.14.10370
- Boeuf, S., Steck, E., Pelttari, K., Hennig, T., Buneß, A., Benz, K., Witte, D., Sülthmann, H., Poustka, A. and Richter, W.** (2008). Subtractive gene expression profiling of articular cartilage and mesenchymal stem cells: Serpins as cartilage-relevant differentiation markers. *Osteoarthr. Cartil.* **16**, 48–60. doi:10.1016/j.joca.2007.05.008
- Cao, L., Guilak, F. and Setton, L. A.** (2009). Pericellular matrix mechanics in the anulus fibrosus predicted by a three-dimensional finite element model and in situ morphology. *Cell. Mol. Bioeng.* **2**, 306–319. doi:10.1007/s12195-009-0081-7
- Cao, L., Guilak, F. and Setton, L. A.** (2011). Three-dimensional finite element modeling of pericellular matrix and cell mechanics in the nucleus pulposus of the intervertebral disk based on in situ morphology. *Biomech. Model. Mechanobiol.* **10**, 1–10. doi:10.1007/s10237-010-0214-x
- Cescon, M., Gattazzo, F., Chen, P. and Bonaldo, P.** (2015). Collagen VI at a glance. *J. Cell Sci.* **128**, 3525–3531. doi:10.1242/jcs.169748

- Chijimatsu, R., Kunugiza, Y., Taniyama, Y., Nakamura, N., Tomita, T. and Yoshikawa, H.** (2015). Expression and pathological effects of periostin in human osteoarthritis cartilage. *BMC Musculoskelet. Disord.* **16**, 215. doi:10.1186/s12891-015-0682-3
- Costell, M., Gustafsson, E., Aszódi, A., Mörgelin, M., Bloch, W., Hunziker, E., Addicks, K., Timpl, R. and Fässler, R.** (1999). Perlecan maintains the integrity of cartilage and some basement membranes. *J. Cell Biol.* **147**, 1109–1122. doi:10.1083/jcb.147.5.1109
- Cox, J. and Mann, M.** (2008). MaxQuant enables high peptide identification rates, individualized p.p.b.-range mass accuracies and proteome-wide protein quantification. *Nat. Biotechnol.* **26**, 1367. doi:10.1038/nbt.1511
- Cox, J., Hein, M. Y., Luber, C. A., Paron, I., Nagaraj, N. and Mann, M.** (2014). Accurate proteome-wide label-free quantification by delayed normalization and maximal peptide ratio extraction, termed MaxLFQ. *Mol. Cell. Proteomics* **13**, 2513–2526. doi:10.1074/mcp.M113.031591
- Eyre, D. R., Brickley-Parsons, D. M. and Glimcher, M. J.** (1978). Predominance of type I collagen at the surface of avian articular cartilage. *FEBS Lett.* **85**, 259–263. doi:10.1016/0014-5793(78)80468-2
- Farach-Carson, M. C., Warren, C. R., Harrington, D. A. and Carson, D. D.** (2014). Border patrol: Insights into the unique role of perlecan/heparan sulfate proteoglycan 2 at cell and tissue borders. *Matrix Biol.* **34**, 64–79. doi:10.1016/j.matbio.2013.08.004
- Flanagan-Steet, H., Christian, C., Lu, P.-N., Aarnio-Peterson, M., Sanman, L., Archer-Hartmann, S., Azadi, P., Bogyo, M. and Steet, R. A.** (2018). TGF-beta regulates cathepsin activation during normal and pathogenic development. *Cell Rep.* **22**, 2964–2977. doi:10.1016/j.celrep.2018.02.066
- French, M. M., Smith, S. E., Akanbi, K., Sanford, T., Hecht, J., Farach-Carson, M. C. and Carson, D. D.** (1999). Expression of the heparan sulfate proteoglycan, perlecan, during mouse embryogenesis and perlecan chondrogenic activity in vitro. *J. Cell Biol.* **145**, 1103–1115. doi:10.1083/jcb.145.5.1103
- Gelse, K., Pöschl, E. and Aigner, T.** (2003). Collagens-structure, function, and biosynthesis. *Adv. Drug Deliv. Rev.* **55**, 1531–1546. doi:10.1016/j.addr.2003.08.002
- Gomes, R., Kirn-Safran, C., Farach-Carson, M. C. and Carson, D. D.** (2002). Perlecan: An important component of the cartilage pericellular matrix. *J. Musculoskelet. Neuronal Interact.* **2**, 511–516.
- Gubbiotti, M. A., Neill, T. and Iozzo, R. V.** (2017). A current view of perlecan in physiology and pathology: A mosaic of functions. *Matrix Biol.* **57–58**, 285–298. doi:10.1016/j.matbio.2016.09.003
- Guilak, F., Alexopoulos, L. G., Upton, M. L., Youn, I., Choi, J. B., Cao, L., Setton, L. A. and Haider, M. A.** (2006). The pericellular matrix as a transducer of biomechanical and biochemical signals in articular cartilage. In *Annals of the New York Academy of Sciences*, pp. 498–512. Blackwell Publishing Inc.
- Guo, H., Maher, S. A. and Torzilli, P. A.** (2014). A biphasic multiscale study of the mechanical microenvironment of chondrocytes within articular cartilage under unconfined compression. *J. Biomech.* **47**, 2721–2729. doi:10.1016/j.jbiomech.2014.05.001
- Han, L., Grodzinsky, A. J. and Ortiz, C.** (2011). Nanomechanics of the cartilage extracellular matrix. *Annu. Rev. Mater. Res.* **41**, 133–168. doi:10.1146/annurev-matsci-062910-100431

- Heinegård, D., Lorenzo, P., Önnerfjord, P. and Saxne, T.** (2015). Articular cartilage. In *Rheumatology* (ed. Hochberg, M. C., Silman, A. J., Smolen, J. S., Weinblatt, M. E., and Weisman, M. H. B. T.-R.), (Sixth E.), pp. 33–41. Philadelphia: Mosby
- Hoemann, C. D.** (2004). Molecular and biochemical assays of cartilage components. *Methods Mol. Med.* **101**, 127–156. doi:10.1385/1592598218
- Hopf, M., Göhring, W., Kohfeldt, E., Yamada, Y. and Timpl, R.** (1999). Recombinant domain IV of perlecan binds to nidogens, laminin-nidogen complex, fibronectin, fibulin-2 and heparin. *Eur. J. Biochem.* **259**, 917–926. doi:10.1046/j.1432-1327.1999.00127.x
- Hsueh, M.-F., Khabut, A., Kjellström, S., Önnerfjord, P. and Kraus, V. B.** (2016). Elucidating the molecular composition of cartilage by proteomics. *J. Proteome Res.* **15**, 374–388. doi:10.1021/acs.jproteome.5b00946
- Iacobini, C., Fantauzzi, C. B., Pugliese, G. and Menini, S.** (2017). Role of galectin-3 in bone cell differentiation, bone pathophysiology and vascular osteogenesis. *Int. J. Mol. Sci.* **18**, 2481. doi:10.3390/ijms18112481
- Ishida, K., Acharya, C., Christiansen, B. A., Yik, J. H. N., DiCesare, P. E. and Haudenschild, D. R.** (2013). Cartilage oligomeric matrix protein enhances osteogenesis by directly binding and activating bone morphogenetic protein-2. *Bone* **55**, 23–35. doi:10.1016/j.bone.2013.03.007
- Ishijima, M., Suzuki, N., Hozumi, K., Matsunobu, T., Kosaki, K., Kaneko, H., Hassell, J. R., Arikawa-Hirasawa, E. and Yamada, Y.** (2012). Perlecan modulates VEGF signaling and is essential for vascularization in endochondral bone formation. *Matrix Biol.* **31**, 234–245. doi:10.1016/j.matbio.2012.02.006
- Jin, H. and Lewis, J. L.** (2004). Determination of Poisson's ratio of articular cartilage by indentation using different-sized indenters. *J. Biomech. Eng.* **126**, 138–145. doi:10.1115/1.1688772
- Kesava Reddy, G. and Enwemeka, C. S.** (1996). A simplified method for the analysis of hydroxyproline in biological tissues. *Clin. Biochem.* **29**, 225–229. doi:10.1016/0009-9120(96)00003-6
- Knott, L. and Bailey, A. J.** (1998). Collagen cross-links in mineralizing tissues: A review of their chemistry, function, and clinical relevance. *Bone* **22**, 181–187. doi:10.1016/S8756-3282(97)00279-2
- Kvist, A. J., Johnson, A. E., Mörgelin, M., Gustafsson, E., Bengtsson, E., Lindblom, K., Aszódi, A., Fässler, R., Sasaki, T., Timpl, R., et al.** (2006). Chondroitin sulfate perlecan enhances collagen fibril formation: Implications for perlecan chondrodysplasias. *J. Biol. Chem.* **281**, 33127–33139. doi:10.1074/jbc.M607892200
- Leijten, J. C. H., Bos, S. D., Landman, E. B. M., Georgi, N., Jahr, H., Meulenbelt, I., Post, J. N., van Blitterswijk, C. A. and Karperien, M.** (2013). GREM1, FRZB and DKK1 mRNA levels correlate with osteoarthritis and are regulated by osteoarthritis-associated factors. *Arthritis Res. Ther.* **15**, R126–R126. doi:10.1186/ar4306
- Liu, B., Lad, N. K., Collins, A. T., Ganapathy, P. K., Utturkar, G. M., McNulty, A. L., Spritzer, C. E., Moorman, C. T., Sutter, E. G., Garrett, W. E., et al.** (2017). In vivo tibial cartilage strains in regions of cartilage-to-cartilage contact and cartilage-to-meniscus contact in response to walking. *Am. J. Sports Med.* **45**, 2817–2823. doi:10.1177/0363546517712506
- Long, F. and Linsenmayer, T. F.** (1998). Regulation of growth region cartilage proliferation and differentiation by perichondrium. *Development* **125**, 1067–1073.

- Lorent, K., Overbergh, L., Delabie, J., Van Leuven, F. and Van den Berghe, H.** (1994). Distribution of mRNA coding for Alpha-2-macroglobulin, the murinoglobulins, the Alpha-2-macroglobulin receptor and the Alpha-2-macroglobulin receptor associated protein during mouse embryogenesis and in adult tissues. *Differentiation* **55**, 213–223. doi:10.1046/j.1432-0436.1994.5530213.x
- Lycke, R. J., Walls, M. K. and Calve, S.** (2019). Computational modeling of developing cartilage using experimentally derived geometries and compressive moduli. *J. Biomech. Eng.* **141**, 81002–81008. doi:10.1115/1.4043208
- Martinez, J. R., Grindel, B. J., Hubka, K. M., Dodge, G. R. and Farach-Carson, M. C.** (2019). Perlecan/HSPG2: Signaling role of domain IV in chondrocyte clustering with implications for Schwartz-Jampel Syndrome. *J. Cell. Biochem.* **120**, 2138–2150. doi:10.1002/jcb.27521
- Mi, H., Muruganujan, A., Ebert, D., Huang, X. and Thomas, P. D.** (2018). PANTHER version 14: more genomes, a new PANTHER GO-slim and improvements in enrichment analysis tools. *Nucleic Acids Res.* **47**, D419–D426. doi:10.1093/nar/gky1038
- Miedel, E. L., Brisson, B. K., Hamilton, T., Gleason, H., Swain, G. P., Lopas, L., Dopkin, D., Perosky, J. E., Kozloff, K. M., Hankenson, K. D., et al.** (2015). Type III collagen modulates fracture callus bone formation and early remodeling. *J. Orthop. Res.* **33**, 675–684. doi:10.1002/jor.22838
- Miosge, N., Sasaki, T. and Timpl, R.** (2002). Evidence of nidogen-2 compensation for nidogen-1 deficiency in transgenic mice. *Matrix Biol.* **21**, 611–621. doi:10.1016/S0945-053X(02)00070-7
- Naba, A., Clauser, K. R., Hoersch, S., Liu, H., Carr, S. A. and Hynes, R. O.** (2012). The matrisome: in silico definition and in vivo characterization by proteomics of normal and tumor extracellular matrices. *Mol. Cell. Proteomics* **11**. doi:10.1074/mcp.M111.014647
- Naba, A., Pearce, O. M. T., Del Rosario, A., Ma, D., Ding, H., Rajeeve, V., Cutillas, P. R., Balkwill, F. R. and Hynes, R. O.** (2017). Characterization of the extracellular matrix of normal and diseased tissues using proteomics. *J. Proteome Res.* **16**, 3083–3091. doi:10.1021/acs.jproteome.7b00191
- Nessler, M., Puchala, J., Kwiatkowski, S., Kobylarz, K., Mojsa, I. and Chrapusta-Klimeczek, A.** (2011). Multidisciplinary approach to the treatment of a patient with chondrodystrophic myotonia (Schwartz-Jampel vel Aberfeld Syndrome). *Ann. Plast. Surg.* **67**, 315–319. doi:10.1097/sap.0b013e3181fac1ec
- Newman, B., Gigout, L. I., Sudre, L., Grant, M. E. and Wallis, G. A.** (2001). Coordinated expression of matrix Gla protein is required during endochondral ossification for chondrocyte survival. *J. Cell Biol.* **154**, 659–666. doi:10.1083/jcb.200106040
- Nicole, S., Davoine, C.-S., Topaloglu, H., Cattolico, L., Barral, D., Beighton, P., Hamida, C. Ben, Hammouda, H., Cruaud, C., White, P. S., et al.** (2000). Perlecan, the major proteoglycan of basement membranes, is altered in patients with Schwartz-Jampel syndrome (chondrodystrophic myotonia). *Nat. Genet.* **26**, 480. doi:10.1038/82638
- Ocken, A. R., Ku, M., Kinzer-Ursem, T. L. and Calve, S.** (2019a). Hspg2C1532YNeo DBA distal humeral cartilage proteomic comparison dataset. doi:10.25345/C5BT0W
- Ocken, A. R., Ku, M., Kinzer-Ursem, T. L. and Calve, S.** (2019b). Hspg2C1532YNeo DBA distal humeral cartilage secretome proteomic comparison. doi:10.25345/C5Z66J
- Okamura, N., Hasegawa, M., Nakoshi, Y., Iino, T., Sudo, A., Imanaka-Yoshida, K., Yoshida, T. and Uchida, A.** (2010). Deficiency of tenascin-C delays articular cartilage repair in mice. *Osteoarthr. Cartil.* **18**, 839–848. doi:https://doi.org/10.1016/j.joca.2009.08.013

- Rodgers, K. D., Sasaki, T., Aszodi, A. and Jacenko, O.** (2007). Reduced perlecan in mice results in chondrodysplasia resembling Schwartz–Jampel syndrome. *Hum. Mol. Genet.* **16**, 515–528. doi:10.1093/hmg/ddl484
- Rueden, C. T., Schindelin, J., Hiner, M. C., DeZonia, B. E., Walter, A. E., Arena, E. T. and Eliceiri, K. W.** (2017). ImageJ2: ImageJ for the next generation of scientific image data. *BMC Bioinformatics* **18**, 529. doi:10.1186/s12859-017-1934-z
- Saleh, A. M., Jacobson, K. R., Kinzer-Ursem, T. L. and Calve, S.** (2019). Dynamics of non-canonical amino acid-labeled intra- and extracellular proteins in the developing mouse. *Cell. Mol. Bioeng.* **12**, 495–509. doi:10.1007/s12195-019-00592-1
- Samsa, W. E., Zhou, X. and Zhou, G.** (2017). Signaling pathways regulating cartilage growth plate formation and activity. *Semin. Cell Dev. Biol.* **62**, 3–15. doi:10.1016/j.semcdb.2016.07.008
- Schindelin, J., Arganda-Carreras, I., Frise, E., Kaynig, V., Longair, M., Pietzsch, T., Preibisch, S., Rueden, C., Saalfeld, S., Schmid, B., et al.** (2012). Fiji: an open-source platform for biological-image analysis. *Nat. Methods* **9**, 676. doi:10.1038/nmeth.2019
- Shu, C. C., Smith, S. M., Little, C. B. and Melrose, J.** (2019). Elevated hypertrophy, growth plate maturation, glycosaminoglycan deposition, and exostosis formation in the Hspg2 exon 3 null mouse intervertebral disc. *Biochem. J.* **476**, 225–243. doi:10.1042/BCJ20180695
- Starborg, T., Kalson, N. S., Lu, Y., Mironov, A., Cootes, T. F., Holmes, D. F. and Kadler, K. E.** (2013). Using transmission electron microscopy and 3View to determine collagen fibril size and three-dimensional organization. *Nat. Protoc.* **8**, 1433. doi:10.1038/nprot.2013.086
- Stum, M., Girard, E., Bangratz, M., Bernard, V., Herbin, M., Vignaud, A., Ferry, A., Davoine, C.-S., Echaniz-Laguna, A., René, F., et al.** (2008). Evidence of a dosage effect and a physiological endplate acetylcholinesterase deficiency in the first mouse models mimicking Schwartz–Jampel syndrome neuromyotonia. *Hum. Mol. Genet.* **17**, 3166–3179. doi:10.1093/hmg/ddn213
- Tashima, T., Nagatoishi, S., Sagara, H., Ohnuma, S. and Tsumoto, K.** (2015). Osteomodulin regulates diameter and alters shape of collagen fibrils. *Biochem. Biophys. Res. Commun.* **463**, 292–296. doi:10.1016/j.bbrc.2015.05.053
- Tillgren, V., Ho, J. C. S., Önnarfjord, P. and Kalamajski, S.** (2015). The novel small leucine-rich protein chondroadherin-like (CHADL) is expressed in cartilage and modulates chondrocyte differentiation. *J. Biol. Chem.* **290**, 918–925. doi:10.1074/jbc.M114.593541
- Trickey, W. R., Baaijens, F. P. T., Laursen, T. A., Alexopoulos, L. G. and Guilak, F.** (2006). Determination of the Poisson’s ratio of the cell: Recovery properties of chondrocytes after release from complete micropipette aspiration. *J. Biomech.* **39**, 78–87. doi:10.1016/j.jbiomech.2004.11.006
- Turk, V., Stoka, V., Vasiljeva, O., Renko, M., Sun, T., Turk, B. and Turk, D.** (2012). Cysteine cathepsins: From structure, function and regulation to new frontiers. *Biochim. Biophys. Acta* **1824**, 68–88. doi:10.1016/j.bbapap.2011.10.002
- Vincent, T. L., McLean, C. J., Full, L. E., Peston, D. and Saklatvala, J.** (2007). FGF-2 is bound to perlecan in the pericellular matrix of articular cartilage, where it acts as a chondrocyte mechanotransducer. *Osteoarthr. Cartil.* **15**, 752–763. doi:10.1016/j.joca.2007.01.021
- Wilson, R., Norris, E. L., Brachvogel, B., Angelucci, C., Zivkovic, S., Gordon, L., Bernardo, B. C., Stermann, J., Sekiguchi, K., Gorman, J. J., et al.** (2012). Changes in the chondrocyte and extracellular matrix proteome during post-natal mouse cartilage development. *Mol. Cell. Proteomics* **11**. doi:10.1074/mcp.M111.014159

- Wilson, R., Golub, S. B., Rowley, L., Angelucci, C., Karpievitch, Y. V., Bateman, J. F. and Fosang, A. J.** (2016). Novel elements of the chondrocyte stress response identified using an in vitro model of mouse cartilage degradation. *J. Proteome Res.* **15**, 1033–1050. doi:10.1021/acs.jproteome.5b01115
- Wilusz, R. E., DeFrate, L. E. and Guilak, F.** (2012). A biomechanical role for perlecan in the pericellular matrix of articular cartilage. *Matrix Biol.* **31**, 320–327. doi:10.1016/j.matbio.2012.05.002
- Xu, X., Li, Z., Cai, L., Calve, S. and Neu, C. P.** (2016a). Mapping the nonreciprocal micromechanics of individual cells and the surrounding matrix within living tissues. *Sci. Rep.* **6**, 24272. doi:10.1038/srep24272
- Xu, X., Li, Z., Leng, Y., Neu, C. P. and Calve, S.** (2016b). Knockdown of the pericellular matrix molecule perlecan lowers in situ cell and matrix stiffness in developing cartilage. *Dev. Biol.* **418**, 242–247. doi:10.1016/j.ydbio.2016.08.029